Hematite Dysprosium Oxide (Fe_2O_3–Dy_2O_3) Nanocomposites for Antibiotic and Microorganism Removals from Surface Water

RUKİYE ÖZTEKİN, DELİA TERESA SPONZA*
Department of Environmental Engineering
Dokuz Eylül University
Tınaztepe Campus, 35160 Buca/Izmir,
TURKEY

**Corresponding Author*

Abstract: - In this study, hematite dysprosium oxide (Fe2O3–Dy2O3) nanocomposites was generated under laboratory conditions for antibiotic and microorganism removals from the surface water. The effects of increasing nanocomposite concentration, Chloramphenicol (Chloram) antibiotic doses, time and ionic strength levels on the adsorption yields of antibiotic, bacteria (E. coli, Pseudomonas and Salmonella) and virus (Enteric viruses) were investigated. Fe2O3–Dy2O3 (FD) was synthesized via green approach using Syzygium aromaticum bud extract. The formation of Fe2O3–Dy2O3 nanocomposite was confirmed by FTIR, XRD, XPS, FESEM, TEM, VSM, EDX, BET, TGA, and ODRS analyses. A magnetic counterpart Fe2O3–Dy2O3 (c-FD) was obtained via calcinations of FD at 700°C and tested for the Chloram removal performance. BET surface area of the FD and c-FD was found to be 112 and 41 m2/g. Antibiotics have been emerged as an issue high concern due to their potential risk for ecosystem and human health. The detailed kinetic and isotherm modelling showed that the Chloram antibiotic adsorption did not match with the pseudo-second-order and the monolayer pseudo first order adsorption kinetics on the surface of FD and c-FD nanocomposites respectively. With Langmuir and Freundlich adsorption kinetic constants also the Chloram adsorption cannot be defined due to low kinetic constants with low regression coefficients. The removal of Chloram antibiotic in FD and c-FD nanocomposites can be explained with intraparticle diffusion kinetic with high intraparticle diffusion rate constant (Kid) values of 0.982 and 1.98 for 0.001 mg/l Chloram up to 40 mg/l, respectively in both nanocomposites, respectively, with low boundary layer thickness C (0.08 mg/g) values and with high R2 values of 0.999. The maximum removal percentage of Chloram was found to be 99% for FD and 96% for c-FD nanocomposites at an adsorbent dose of 2 mg/l within 15 min for 40 ppm initial concentration of Chloram at an ionic strength of 1.2 M. As the ionic strength was increased from 0.01 M up to 1.2 M, the adsorption efficiencies of Chloram antibiotic increased from 90% and 82% up to 99% and 87%, in FD and c-FD nanocomposites, respectively. The Chloram antibiotic yields at low Chloram concentrations also simulating the surface water doses (0.0001 mg/l, 0.001 and 0.01 mg/l) were 99% at FD nanocomposite.At high Chloram concentrations also (40 mg/l) the Chloram yields also was detected as 99% at FD nanocomposites. The effect of FD and c-FD nanocomposites on bacterial strains (E. coli, Pseudomonas and Salmonella and viruses (Enteric viruses) were found to be high. The removal efficiencies of microorganisms from surface waters using Fe2O3–Dy2O3 nanocomposites are ranked as follows: E. coli > Pseudomonas > Enteric viruses > Salmonella, respectively. The reuse of Fe2O3–Dy2O3 nanocomposite was also investigated. The recyclability of the aforementioned nanoadsorbents showed excellent cycling stability and reuse properties. The operational stability of both nano-adsorbents was revealed by evaluating the Chloram (40 ppm) adsorption after 70 cycle runs. Until 70 cycles the Chloram yields were 99% and 96% at FD and c-FD nanocomposites, respectively. After 70 cycles the Chloram yields decreased slightly to 88% and 80%. This is very advanantageous for further application in water purification and treatment.

Key-Words: - Adsorption capacity; Antibiotics; Bacteria; Chloramphenicol (Chloram); Hematite dysprosium oxide (Fe2O3–Dy2O3) nanocomposites; Microorganisms; Pathogens; Reuse; Surface water; Virus.

Received: March 22, 2026. Revised: April 3, 2026. Accepted: April 15, 2026. Published: July 14, 2026.

1 Introduction

Antibiotics have become an important water pollutant owing their intense use over the past decades, [1]. Since their introduction in 1950, Choramphenicols are one of the major types of antibiotics, besides sulfonamides, macrolides, and quinolones that have been extensively used in human and veterinary medicines and as growth promoters in agriculture and aquaculture, [2], [3].

The generation Chloramphenicols were approved by the Food and Drug Administration in 2005 and after a decade of clinical use, remain relatively active against many multidrug resistance pathogens including Staphylococcus aureus, Acinetobacter baumannii, Klebsiella pneumoniae, and Escherichia coli., [4], [5]. There are many pathways for the environmental release of antibiotics, but in general, any anthropogenic activity which demands its use has exposed it to the contamination of soils and sediments and passed it to subsurface water, lakes, and rivers.

The removals of bacteria, viruses and antibiotics via nanocomposites can be explained as follows:

Physical trapping and surface interaction: The mesoporous structure of the nanocomposite offers a large surface area for the retention of pathogens. However, the differences in ranking are based on the following physical factors: (a) Size and form matching: Bacteria such as E. coli and Pseudomonas possess structures like flagella and fimbriae that facilitate attachment to mesoporous surfaces. Studies have shown that these structures can establish specific ligand-receptor bonds with functional groups on nanocomposite surfaces (e.g., N-acetylglucosamine in chitosan-coated systems). (b) Electrostatic attraction: Hematite (α-Fe_2O_3)-based structures can have a positive surface charge depending on the pH value. The electrostatic attraction between negatively charged bacterial cell walls (especially Gram-negatives) and this positive surface maximizes adhesion.

The true antimicrobial effect of dysprosium addition: Removal is not just "imprisonment," but an active elimination process. Dysprosium (Dy) addition enhances the natural catalytic properties of hematite in the following ways: (a) Reactive oxygen species (ROS) production: Dysprosium improves the separation of electron-hole pairs by creating defects in the hematite structure. This increases the production of potent oxidizers such as hydroxyl radicals ($OH^{\bullet}$) and super oxides ($O^{-}{}^{2\bullet}$) in an aqueous environment. (b) Cell wall degradation: These produced reactive oxygen species (ROS) kill the cell by causing lipid peroxidation and protein damage, especially in species whose cell wall structure is more susceptible to ROS attacks, such as E. coli.

Reasons for the ranking of microorganisms: It is removed most efficiently via both strong electrostatic attraction and excellent chemical compatibility with the nanocomposite surface of structures like F-17 fimbriae. (a) Pseudomonas: Efficiently retained due to high adaptability and biofilm-forming tendency, but may be slightly more resistant to ROS than E. coli. (b) Enteric viruses: Their very small size (nano meter level) makes them difficult to trap through mechanical straining like bacteria. They lag behind bacteria as their removal relies almost entirely on electrostatic attraction. (c) Salmonella: Salmonella cells are generally larger than E. coli, and structures like SiiE adhesin on their surface may require a greater distance to approach the nanocomposite surface. This reduces the number of bacteria retained per unit mass (adsorption capacity).

This removal process begins with physical adsorption in the mesopores and the addition of dysprosium, transforms into a sustained antimicrobial effect through oxidative stress (ROS).

Surface water is prone to bacterial contamination as it receives wastes and pollutants from human and animal sources, and contaminated water may expose local populations to health risks. This provides on the prevalence and antimicrobial resistance phenotypes of Salmonella, Escherichia coli and Enterococcus, found in natural freshwaters. These bacteria are frequently detected in surface waters, sometimes as etiological agents of waterborne infections, and antimicrobial resistance strains are not uncommonly identified in both developed and developing countries. Data relating to Salmonella, E. coli and Enterococcus present in environmental water are lacking, and in order to understand their development and dissemination using the One Health approach, understanding the prevalence, distribution and characteristics of the bacteria present in surface water as well as their potential sources is important. Furthermore, antimicrobial resistance bacteria in natural watersheds are not well investigated and their impacts on human health and food safety are not well understood. As surface water is a receptacle for antimicrobial resistance bacteria from human and animal sources and a vehicle for their dissemination, this is a crucial data gap in understanding antimicrobial resistance and minimizing its spread. Salmonella, E. coli and Enterococcus were chosen to evaluate the presence of primary pathogens and opportunistic pathogens as well as to monitor antimicrobial resistance trends in the environmental water. In the literature studies around the world have demonstrated the widespread distribution of pathogenic and antimicrobial resistance bacteria in surface waters of both developing and developed

countries, confirming the importance of environmental waters as a reservoir for these bacteria and the need for more attention on the environmental bacteria for emerging antimicrobial resistance.

Studies have warned about the potential ecological risks and public health threat, [6], [7]. The occurrence of Chloramphenicols in surface water and soils is becoming a worldwide issue, and the toxicity effect eventually will reach the ecosystems, [8], [9], [10]. The more significant techniques to remove micropollutants from contaminated media include adsorption, biodegradation, photodegradation, and the advanced oxidation process.

Some of them face many challenges due to their high operational costs and time-consuming processes, [11], [12], [13]. Adsorption is an inexpensive technique easy to implement, with high efficiency, and without toxic by-products, [14], [15], [16], [17]. The effectiveness of the adsorption process depends on the physicochemical properties of the adsorbent, such as specific surface area, porosity, surface polarity, and morphology of the material, as well as the characteristics of the adsorbate, such as size, polarity, ionic charge, and hydrophobicity, [18], [19]. The adsorption mechanisms consist of the electrostatic interaction and physical bindings of adsorbate to the specific sites on the surface of an adsorbent, [20]. Activated carbons are frequently used as adsorbent owing to the high specific surface area, pore size, and chemical functionalities, [21], [22], [23].

Pharmaceutical run of has been considered as one of the most noxious effluents due to their incessant loading and persistence even at low concentrations in the water bodies, [24], [25], [26]. The prolonged exposure to antibiotics causes the emergence of new multidrug-resistant pathogenic bacteria, [27], [28].

The release of untreated and partially treated pharmaceutical waste into the drinking water and other water sources results in polluting the water, [29], [30]. Pharmaceutical waste includes a variety of chemical compounds like antipyretics, analgesics, steroids, antihypertensive, antidepressants, contraceptives, antibiotics, etc, [31], [32], [33], [34]. Although, the concentration of these compounds is relatively low (mg/l to µg/l) but still they are highly hazardous for humans and aquatic organisms, [35], [36], [37], [38].

There are extensive treatment methods available to treat antibiotic-contaminated water, such as biodegradation, chemical oxidation, photocatalytic degradation and adsorption, [39], [40], [41]. Each of them has its own advantages and limitations like use of harmful chemical oxidizing agents, formation of toxic byproducts, high operational cost, and low efficiency, [42], [43]. Out of these developed methods, adsorption is the widely exploited methodology for the removal of pollutants owing to its simplicity, less toxicity and cost-effectiveness, [44], [45]. Recent studies conveyed that besides natural materials, such as soil and clay, the engineered nanomaterials, i.e. metal oxide nanoparticles and metal organic framework have displayed strong adsorption capacities for antibiotics removal due to their highly porous structure with microporous/mesoporous cavities, [46], [47].

However, metal oxides have been less explored due to the toxicity issues associated with them. There are other disadvantages also, such as high-temperature synthesis and low separation efficiency, [48], [49], [50]. Therefore, the development of highly efficient, easily recyclable adsorbents with low toxicity is highly desirable, [51], [52], [53].

Among many transition metal oxides, hematite (α-Fe_2O_3) has been a widely studied nanomaterial due to its internal porosity with additional benefit of simple separation under influence of external magnetic field, low cost and environmentally friendly nature, [54]. Owing to these properties, it is used in a variety of environmental applications, such as catalysis, sensing and adsorption, [54].

Several iron-based nanomaterials have been utilized for the efficient removal of antibiotic-based contaminants, such as metoprolol, carbamazepine, ciprofloxacin, tetracyclines, chloramphenicol, etc, [55]. Recently, the use of metal oxide-based nano-adsorbents prepared using green methodology has gained considerable attention due to their non-toxicity, cost effectiveness, and eco-friendly nature, [31]. There are several reports where plant extract or microorganisms have been exploited to produce metal oxide nanocomposites, [56]. The process is free from harmful chemicals, i.e. reducing and stabilizing agents as the biological moieties present in the plant extract itself act as reducing and stabilizing agents for nanoparticles, [56]. A variety of these nanoparticles have found their applications in the field of adsorption, catalysis, batteries, etc.

Despite the progress in this field there is huge scope for improvement in adsorption performances of haematite nanocomposites, [57]. Hence, the chemists are trying to enhance the adsorption capacity of haematite- based adsorbents by simple and cost-effective techniques, [57]. Besides, it is advantageous to explore the green route, low-cost methods for large-scale production of nanocomposites by exploring natural ingredients as they are present in ample amount and low toxicity.

Metal/metal oxide incorporation in matrix of other oxides is found to be effective in enhancing the adsorption efficiency of host system, [58], [59]. The physicochemical properties of nanomaterials are

remarkably influenced leading them to be suitable for a variety of technical applications.

Chloramphenicol (Chloram); an effective broad-spectrum antibiotic with excellent antibacterial properties, has been widely used to inhibit both gram-positive and gram- negative bacteria in humans and other mammals, [54], [60]. Excessive usage of Chloram may result in bone marrow depression, fatal aplastic anaemia, gray baby syndrome in humans, etc, [61], [62], [63]. Consequently, Chloram has been banned by many developed countries for use in food-producing animals, [64], [65], [66]. However, Chloram is still widely used in many developing countries due to its low cost and availability, leading to water and soil pollution and increase in microbial resistance. The structure of chloramphenicol (M_W=323.13 g/mol) was determined in Figure 1.

*Figure 1 can be found in the Appendix section.

Chloramphenicol is an antibiotic useful for the treatment of a number of bacterial infections,[67]. This includes use as an eye ointment to treat conjunctivitis, [68]. By mouth or by injection into a vein, it is used to treat meningitis, plague, cholera, and typhoid fever, [67]. Its use by mouth or by injection is only recommended when safer antibiotics cannot be used, [67]. Monitoring both blood levels of the medication and blood cell levels every two days is recommended during treatment, [67].

Common side effects include bone marrow suppression, nausea, and diarrhea, [67]. The bone marrow suppression may result in death, [67]. To reduce the risk of side effects treatment duration should be as short as possible, [68]. People with liver or kidney problems may need lower doses, [67]. In young infants, a condition known as gray baby syndrome may occur which results in a swollen stomach and low blood pressure, [67]. Its use near the end of pregnancy and during breastfeeding is typically not recommended, [69]. Chloramphenicol is a broad-spectrum antibiotic that typically stops bacterial growth by stopping the production of proteins, [67].

The biosynthesis of Chloramphenicol is the biosynthetic gene cluster and pathway for chloroamphenicol was characterized from Streptomyces venezuelae ISP5230 (ATCC 17102), [70], [71], [72]. Currently the chloramphenicol biosynthetic gene cluster has 17 genes with assigned roles, [73].

Hematite (α-Fe_2O_3) has been the focus of various theoretical and experimental studies, owing to its applications as a magnetic, semiconductor and catalytic material. Doping hematite with several transition metal and rare earth elements was found to determine an improvement of its electrochemical and photocatalytical properties, [74], [75], [76], [77], [78], [79].

Dysprosium oxide (Dy_2O_3) is a paramagnetic compound that can be used to functionalize α-Fe_2O_3 with prospective applications in sensing, catalysis and flexible electronics. In particular, dysprosium ion Dy^{3+} was found to exhibit intriguing properties when introduced in several systems, [80], [81], [82], [83], [84], [85], [86], [87], [88], [89], [90], [91], [92], [93], [94], [95]. Thus, α-Fe_2O_3 nanoparticles electrochemically doped with dysprosium cations were found to lead to the development of novel iron-based electrodes, due to their supercapacitive and magnetic properties, [96]. The Dy^{3+} ion was found to present a combined impact on the physical, optical, magnetic and DC-electrical properties of dysprosium doped $Cu_{0.8}Cd_{0.2}Dy_xFe_{2-x}O_4$ nanoferrites, [84]. The effect of Dy replacing Fe on the microstructure, electrical properties and magnetic properties of NiZnCo ferrite was also investigated, [85]. Reference, [87], reports on the effect of dysprosium substitution on the crystal structure and physical properties of multiferroic $BiFeO_3$ ceramics. A Mössbauer study of multiferroic $DyFeO_3$ is available in literature, [89], but the dysprosium orthoferrite investigated was in polycrystalline form rather than nanoparticles.

Recently, the ball milling technique was key to obtaining garnet-graphene nanocomposites, [97], and crucial to determine the formation of skyrmion phase in the Fe-Co-Si system, [98]. Moreover, mechanochemical activation was used to synthesize mixed-oxide nanostructures of the type $_xGd_2O_3$-(1-x) α-Fe_2O_3, [99], and $_xNd_2O_3$-(1-x) α-Fe_2O_3, [100], with the presence of solid solutions in the former and absence of solid solutions in the latter system.

Many studies in literature have established the significant enhancement in adsorption performance of iron oxide nanocomposites upon doping with different metal ions, [25], [101], [102]. A key objective of the present research was to build a quick and eco-friendly method for the fabrication of Fe_2O_3–Dy_2O_3 nanocomposite (FD) employing clove extract (Syzygium aromaticum) for the adsorptive removal of pharmaceutical pollutant, Chloram, [103]. As per our knowledge, there very few investigations on the green synthesis of Fe_2O_3–Dy_2O_3 nanocomposite till date.

1.1 Adsorption Types

1.1.1 Physical-Adsorption

Adsorption is carried out on such surfaces through natural attractive forces or the so-called Vander Waals forces, [103]. This type of adsorption can be in the form of multiple layers of the adsorbent material on

the surface of the adsorbent material when suitable conditions of pressure and temperature are available, [103]. The adsorbent and the adsorbent, which is estimated at less than (40 kj/mol), therefore, this type of adsorption does not need high temperatures and does not require activation energy and occurs at low temperatures similar to the process of condensation of vapours on the surfaces of liquid materials, [102], [103], [104].

Physical adsorption (physi-sorption) involves the use of van der Waals forces as attractive forces between an adsorbent (solid) and an adsorbent (gas molecules) and is characterized by: (a) All gases are subject to adsorption on the surface of a solid, so there is no difference in physical adsorption; (b) The higher the liquefaction capacity of the gas, the greater the physical adsorption it is subjected to; (c) It is considered an inverse phenomenon that depends on pressure and temperature. Conversely, the lower the pressure, the further away the gas molecules are from the surface of the solid; (d) It increases with the increase in temperature and decreases with its decrease, (e) As a result of the increase in the surface area of the porous materials, they are considered one of the best materials for physical adsorption; (f) It happens without the need for any kind of energy.

1.1.2 Chemical Adsorption

This type of adsorption occurs on surfaces that are not electronically unsaturated, as such surfaces tend to form chemical bonds with the atoms or molecules that have been adsorbed. As a first step in the chemical reaction that occurs between the adsorbent surface and the adsorbent material, this type of adsorption needs a high activation energy, as well as the accompanying temperatures are high and estimated in a quantity greater than (40 kj/mol), and this type of adsorption is specific and is not reversed and limited by its layer Oxygen adsorption on coal surface, hydrogen chloride adsorption on iron surface. The Factors affecting on Adsorption, [101, [103], [104].

In this type of adsorption, the attractive forces between the adsorbent and the adsorbent are in the form of chemical bonds formed within a single-molecule layer, and this process is characterized by the following [98], [99], [100], [101], [102], [103], [104]: (a) For its occurrence, a chemical bond is required to form between the adsorbent and the adsorbent; (b) It occurs slowly at lower temperatures, and increases in frequency with increased pressure; (c) It relates to the surface area with which the greater the adsorption; (d) Unlike physical adsorption; It needs specific energy to stimulate it; (e) Fields of use of adsorption phenomenon; (f) Scientists rely on this phenomenon when their work requires them to find a vacuum, and reactive coal is usually used; (g) Coal miners use masks against toxic gases; Which depends on this phenomenon to purify the air of these gases; (h) When some works impose the absence of moisture in the place, a gel made of aluminium and silica is used, which is able to absorb moisture through adsorption; (j) Adsorption-capable charcoal is used to break up inert gases; (k) In the medical fields, pharmaceutical drugs can kill germs through this phenomenon; (m) Usually, the colour of the sugar is removed by adding charcoal, which is able to adsorb these colours; (n) It is also used in the paint industry to get rid of inert gases, as it will affect the ability of the paint to adhere well to the surface.

1.1.3 Comparison of Physical and Chemical Adsorption

Physisorption, while characterized by weak intermolecular forces and negative enthalpy ($\Delta H^o < 0$, exothermic), can present as kinetically controlled due to slow pore diffusion or mass transfer limitations, rather than high chemical activation energy. The exothermic nature is reconciled with kinetics because the initial adsorption step releases energy, while the "rate-limiting" step is often the physical transport of molecules into the adsorbent surface, not the binding itself. Key points on reconciling these processes:

(1). Physical nature: Physisorption is typically fast and reversible, mediated by weak Van der Waals forces, making it inherently exothermic (releasing heat).

(2). Kinetics vs. thermodynamics: A negative defines the thermodynamic drive (products are lower in energy than reactants), while kinetics dictates the rate, which can be limited by diffusion, not bond-breaking.

(3). Diffusion limitations: On porous materials like zeolites, the measured kinetics can be slow, but this is often due to the time taken for molecules to travel into narrow pores, not the breaking of chemical bonds.

(4). Monolayer coverage: For gases, physisorption is often restricted to a monolayer, with energetics comparable to liquefaction.

This phenomenon is often explained through "pseudo" (false) kinetic models and energy barriers. The contradiction between the exothermic nature of physisorption and slow processes resembling a chemical velocity is resolved in three key points:

(a) Activation energy barrier: Although, physisorption theoretically has a low activation energy (E_a), adsorbate molecules encounter steric barriers as they pass through narrow channels in porous structures (activated carbon, zeolite, etc.). This "diffusion resistance" causes the kinetic data to fit a pseudo-second-order model (implying chemical control).

(b) Surface heterogeneity: The energy levels on the adsorbent surface are not homogeneous. It takes time for molecules to settle into the most stable regions and rearrange themselves on the surface. This creates an illusion of "chemical confinement," where the rate depends on the occupancy rate of the active sites on the surface, even though it is thermodynamically physisorption.

(c) The flexibility of the pseudo-second order model: In the literature, the pseudo-second-order kinetic model is generally accepted to simulate not only chemisorption but also the combined effects of film diffusion and intrapore diffusion very well. That is, mathematical agreement does not always mean the mechanism is chemical.

In this study, hematite dysprosium oxide (Fe_2O_3–Dy_2O_3) nanocomposites was investigated for removals of Chloram antibiotic and some microorganism from the surface water. The effects of increasing nanocomposite concentrations, Chloramphenicol (Chloram) antibiotic doses, time and ionic strength on the yields of adsorption capacity for the removals of antibiotic, bacteria and viruses were investigated. In order to simulate the surface water low Chloram antibiotic concentrations (0.0001 mg/l, 0.001 mg/l and 0,01 mg/l) were used while in order to simulate the pharmaceutical/antibiotic industry wastewaters high Chloram concentrations (30 mg/l, 40 mg/l and 60 mg/l) were used. Fe_2O_3–Dy_2O_3 (FD) was synthesized via green approach using Syzygium aromaticum (Clove) bud extract, for the effective removal of an antibiotic Chloramphenicol (Chloram). The formation of Fe_2O_3–Dy_2O_3 nanocomposite was confirmed by FTIR, XRD, XPS, FESEM, TEM, VSM, EDX, BET, TGA, and ODRS analyses. The adsorption of Chloram antibiotic to Fe_2O_3–Dy_2O_3 (FD) and c-FD nanocomposites was investigated using five different kinetic isotherms namely pseudo-first-order, pseudo second-order kinetic, intraparticle diffusion, Langmuir and Freundlich adsorption models. The effect of FD and c-FD nanocomposites on the removal of 3 bacterial strains and an Enterovirus group present in the surface water and the reuse of Fe_2O_3–Dy_2O_3 nanocomposite was also investigated.

2 Materials and Methods

2.1 Synthesis of Fe_2O_3–Dy_2O_3 Nanocomposite

The mixed nano metal oxide was prepared by co-precipitation. For the synthesis of Fe_2O_3–Dy_2O_3 nanocomposite, 10 mM solutions of $FeCl_3$ and $Dy(NO_3)_3$ were mixed in 1/1 ratio, i.e. $FeCl_3$:$Dy(NO_3)_3$. With this ratio the formation of Fe_2O_3–Dy_2O_3 nanocomposite was performed under laboratory conditions.

The nanocomposite was washed twice with water followed by ethanol. Further, Fe_2O_3–Dy_2O_3 nanocomposite was dried to a powder by a rota evaporation. The calcined Fe_2O_3–Dy_2O_3 nanocomposite was obtained via calcination at 700^{o}C for 1 h.

The prepared Fe_2O_3–Dy_2O_3 was defined as FD while the calcinated Fe_2O_3–Dy_2O_3 at 700^{o}C was defined as c-FD. The FESEM images of FD nanocomposites and c-FD nanocomposites were shown in Figure 2.

*Figure 2 can be found in the Appendix section.

Effect of contact time, adsorbent dose, initial concentration of Chloramphenicol and pH was investigated. The amount of Chloram adsorbed, i.e. adsorption capacity of Chloram-Chloramphenicol and (%) removal was calculated by following Eq. (1) and Eq. (2), respectively.

2.1.1 Syzygium Aromaticum Bud Extract

Syzygium aromaticum bud extract, commonly known as clove bud extract, is a tropical evergreen plant belonging to the myrtle family. The extract obtained from the dried flower buds of this plant is widely used in the medical, cosmetic, and food industries.

Key properties and composition: The most notable feature of this extract is its rich bioactive components:

(a) Eugenol: The main component of the extract, providing strong antiseptic, analgesic (pain-relieving), and anti-inflammatory properties.

(b) Strong antioxidant capacity: Cloves are one of the natural sources with the highest antioxidant capacity, fighting free radicals and reducing oxidative stress.

(c) Beta-carotene and vitamins: Contains nutritious elements such as vitamin A and beta-carotene.

Uses and benefits: Clove bud extract is used in various sectors for the following purposes:

(a) Oral and dental health: Due to its antiseptic and anesthetic effects, it is widely preferred for relieving toothaches and treating gum problems.

(b) Skin and hair care: In cosmetic products, it helps prevent hair loss and promote hair growth by increasing blood flow to the scalp. It is also used in anti-acne products due to its antibacterial properties.

(c) Digestive system: It is used in dietary supplements or traditional medicine for its digestive and gas-relieving effects.

(d) Natural preservative: It is valued as a natural preservative agent in the food and cosmetic industries due to its antibacterial and antifungal properties.

Syzygium aromaticum bud extract is a versatile herbal compound containing a high percentage of eugenol, which fights microbes and has analgesic effects.

2.2 Adsorption Experiments

The batch contact procedure was followed to carry out all the adsorption experiments. In brief, the 10 mg of each nano-adsorbent (FD and c-FD) was added to 10 ml of Chloram solutions at room temperature. The mixtures were magnetically stirred for 15 min to attain equilibrium. Further, the suspension was centrifuged at 10,000 RCF "g" to isolate the nano-adsorbent (FD) from the mixture.

The effects of contact time, adsorbent dose, initial concentration of Chloramphenicol and ionic strength on the removals of Chloram and some bacteria and viruses were investigated in FD and c-FD nanocomposites was investigated. The amount of Chloram adsorbed, i.e. adsorption capacity of Chloram-Chloramphenicol and (%) removal was calculated by following Eq. (1) and Eq. (2), respectively. However, the c-FD was separated by magnetic separation.

The mixture was examined by UV–visible spectrophotometer to measure the amount of Chloram in solution. The amount of Chloram adsorbed, i.e. adsorption capacity of Chloram and (%) removal was calculated by following, [104], Eq. (1) and Eq. (2), respectively.

$$q_e = \frac{(C_0 - C_e)V}{C_0} (1)$$

$$Removal\ (\%) = \frac{C_0 - C_e}{C_0} x100 (2)$$

Where, C_o and C_e (mg/l) represent primary Chloramphenicol (Chloram) concentration of in equilibrium, respectively, V is volume of solution (liter) and m (g) is the weight of adsorbents used. All the adsorption experiments were performed in triplicates.

2.4 Characterization of Fe_2O_3–Dy_2O_3 Nanocomposite

2.4.1 Fourier Transform Infrared Spectroscopy (FTIR) Analysis

The incidence of various functional groups in synthesized adsorbents was authenticated by FTIR using Thermo-Scientific, with diode laser which is thermally-controlled in transmittance mode in the range
of 4000–500 cm^{-1}.

The electronic absorption spectrum was measured on a spectrophotometer Hachioji, Tokyo 193-0835, Japan model). For obtaining absorption spectrum (200–500 nm), quartz cuvettes having 1 cm path length with the precision of ± 0.2 nm were employed.

2.4.2 X-Ray Diffraction (XRD) Analysis

The crystallographic features and phase clarity were investigated by X-ray diffraction studies using XRD PANalycital X'pert PRO at scanning rate of 8° min^{-1} using monochromatic Cu-Kα radiation (λ=1.5418 Å, 40 kV, 40 mA).

Data were collected from 5 to 100° 2Θ in steps of 0.0167° at a scan speed of 0.023537° s^{-1}. A 0.04 rad soller slit and a 2° anti-scatter slit were used on the incident side of the beam, while the diffracted beam optics consisted of a 0.04 rad soller slit, a programmable anti-scatter slit, and a nickel filter. Phase identification of crystalline components was carried out using the X'Pert HighScore Plus software package and the International Centre for Diffraction Data (ICDD) powder diffraction file (PDF) database.

The synthesized samples were examined at 2θ from 10° to 80°. Raman spectrum was collected with a Horiba Jobin Yvon-Labram HR UV-Visible NIR (200-1600 nm) Raman microscope spectrometer, using a laser with the wavelength of 512 nm. The Raman spectrum was collected from 10 scans at a resolution of 2 /cm. The zeta potential was measured with a SurPASS Electrokinetic Analyzer (Austria) with a clamping cell at 300 mbar.

2.4.3 X-Ray Photo Spectroscopy (XPS) Analysis

The valence state of the samples was investigated and was analysed using XPS (ESCALAB 250Xi, England). XPS used an Al Kα source and surface chemical composition and reduction state analyses was done, with the core levels recorded using a pass energy of 30 eV (resolution ≈ 0.10 eV). The peak fitting of the individual core-levels was done using XPS-peak 41 software, achieving better fitting and component identification. All binding energies were calibrated to the C 1s peak originating from C–H or C–C groups at 284.6 eV.

2.4.4 Field Emission Scanning Electron Microscope (FESEM) Analysis

Hitachi-SU8010 (15 kV) field emission electron microscopy FE-SEM was employed to analyse the surface morphology of the samples.

2.4.5 Transmission Electron Microscopy (TEM) Analysis

For morphological studies of both adsorbents, transmission electron microscopy (TEM-TECNAI

200 kV) was used. The samples for TEM were prepared by drop-casting the dispersed sample on carbon grid. Sample-coated carbon grid was air-dried before TEM analysis.

2.4.6 Value Stream Mapping (VSM) Analysis

To investigate the magnetic properties of adsorbents, magnetization was measured by varying the applied field on Lake Shore's Vibrating Sample Magnetometer (VSM). In order to explain the magnetic property of Fe_2O_3–Dy_2O_3 nanocomposite, the magnetic hysteresis curve was measured at 25°C. The hysteresis loop exhibits ferromagnetic behaviour with saturation magnetization (Ms) of 2.59 emu/g.

2.4.7 Energy Dispersive X-Ray (EDX) Analysis

To investigate the morphological properties and structure of the synthesized catalyst and the composition of the elements present in the synthesized catalyst; elemental composition of synthesized adsorbents was investigated using BrookerXfash energy-dispersive X-ray spectrophotometer (EDX).

2.4.8 Adsorption-Desorption Analysis

Porosity of samples was analysed by N_2 adsorption and desorption via employing adsorption analyser, BELSORP at 423°K for 15 h.

2.4.9 Brunauer–Emmett–Teller (BET) Analysis

The surface area was calculated using the multipoint Brunauer–Emmett–Teller (BET) method.

2.4.10 Thermal Assessment with Thermogravimetric (TGA) Analysis

On experimental samples, Fe_2O_3–Dy_2O_3 nanocomposites were examined by TGA analysis performed using a Mettler TGA/SDTA 851e (Columbus, Ohio, OH, USA) instrument. 5 mg samples were heated from room temperature (25°C) to 700°C in an N_2(g) atmosphere at heating rates of 10°C/min, 15 and 20°C/min. Then, TGA analysis was performed simultaneously. TGA was conducted on the samples to observe the mass loss with an increase in temperature, utilizing a ramping rate of 10°/min with N_2(g) as the test environment. TGA was employed to quantify the energy absorbed or dissipated during the testing of the samples. Mettler Toledo Star Software was used for evaluating the data. The experiments were repeated three times and the average values of the parameters were taken to ensure the best fit and standard deviations.

2.4.11 Diffuse Reflectance UV-vis Spectra (DRS) Analysis

UV-vis Diffuse reflectance spectroscopy (UV-VIS DRS) of specimens was examined using a SHI-MADZU spectrometer model UV-1240 (ranging from 200–900 nm with $BaSO_4$ as reference). The 100% reflectance standard was $BaSO_4$ (Fisher Scientific, 99.92%). The sample was ground and pressed on top of the reference that was preloaded in the sample cup. Reflectance data were converted to absorption by employing the Kubelka–Munk equation.

According to the single-constant Kubelka–Munk theory, a non-linear function of reflectance of an opaque substrate is proportional to antibiotic concentration, if the surface reflectance is neglected. The Kubelka–Munk equation links a function of reflectance of an antibiotic substrate to the amount of nanocomposite present in the fiber, as shown in, [105], Eq. (3) and Eq. (4):

$$t_{KM} = \frac{(1-r_\infty^2)e^{-\dot{x}}}{1-r_\infty^2 e^{-2\dot{x}}} \quad (3)$$

$$r_{KM} = \frac{r_\infty(1-e^{-2\dot{x}})}{1-r_\infty^2 e^{-2\dot{x}}} \quad (4)$$

Where, $\dot{x}=\sigma L$, $\sigma = \sqrt{K(K+S)}$ and the subscript KM signifies that equations are valid under assumptions as introduces by Kubelka and Munk, [106]. The last equation can also be written as follows, Eq. (5):

$$r_{KM} = r_\infty[1 - t\exp(-\dot{x})] \quad (5)$$

The main shortcoming of Kubelka-Munk Theorem (KMT) is the fact that diffuse absorption (K) and scattering (S) coefficients have no rigorous electrodynamic meaning. Therefore, their calculation from first principles is hardly possible in Eq. (6):

$$\left(\frac{K}{S}\right)_\lambda = \frac{(1-R_{\infty.\lambda})^2}{2xR_{\infty.\lambda}} = \left(\frac{K}{S}\right)_{sub.\lambda} + \sum C_i\alpha_{i.\lambda} \quad (6)$$

Where, $\left(\frac{K}{S}\right)$ and $\left(\frac{K}{S}\right)_{sub.}$ show the Kubelka-Munk function of antibiotic and nanocomposite substrates, $R_{\infty.\lambda}$ gives the reflectance of monochromatic incident light from an opaque material, $\alpha_{i.\lambda}$ is the unit k/s value of antibiotic (slop of K/S versus concentration in the linear region) for a monochromatic radiant power on a given substrate and C shows the antibiotic concentration in the substrate, K and S indicate the coefficients of absorption and scattering of monochromatic light of an opaque substrate, respectively.

2.5 Analytical Procedures

The organisms were measured according to Standard Methos, [107]. Chloramphenicol was measured in high-pressure liquid chromatography (HPLC). The concentrations of Chloramphenicol were performed using a HPLC (Agilent-1100). The samples were analyzed by HPLC with photodiode array and mass spectrometric detection (MSD) using an Agilent 1100 HPLC system consisting of an automatic injector, a gradient pump, a Hewlett–Packard series 1100 photodiode array detector. The chromatographic conditions for the determination of ibuprophene and oxytetracycline concentrations were as follows: C-18 reverse phase HPLC column (Ace 5C18; 25-cm x 4.6-mm, 5 μm, mobile phase: 50/50 (v/v) methanol/organic-free reagent water). The experimental results were detected with an Agilent series 1100 VL on-line atmospheric pressure ionization electrospray ionization mass spectrometer. The bacteria and viruses were analysed according to Standard Methods, [107].

2.6 Resistance Mechanism of Chloramphenicol

Chloramphenicol is a bacteriostatic agent, inhibiting protein synthesis. It prevents protein chain elongation by inhibiting the peptidyl transferase activity of the bacterial ribosome. It specifically binds to A2451 and A2452 residues, [108], in the 23S rRNA of the 50S ribosomal subunit, preventing peptide bond formation, [109]. Chloramphenicol directly interferes with substrate binding in the ribosome, as compared to macrolides, which sterically block the progression of the growing peptide, [110], [111], [112].

Three mechanisms of resistance to chloramphenicol are known: reduced membrane permeability, mutation of the 50S ribosomal subunit, and elaboration of chloramphenicol acetyltransferase. It is easy to select for reduced membrane permeability to chloramphenicol in vitro by serial passage of bacteria, and this is the most common mechanism of low-level chloramphenicol resistance. High-level resistance is conferred by the cat-gene; [113], this gene codes for an enzyme called chloramphenicol acetyltransferase, which inactivates chloramphenicol by covalently linking one or two acetyl groups, derived from acetyl-S-coenzyme A, to the hydroxyl groups on the chloramphenicol molecule. The acetylation prevents chloramphenicol from binding to the ribosome. Resistance-conferring mutations of the 50S ribosomal subunit are rare, [113].

Chloramphenicol resistance may be carried on a plasmid that also codes for resistance to other drugs. One example is the ACCoT plasmid (A=ampicillin, C=chloramphenicol, Co=co-trimoxazole, T=tetracycline), which mediates multiple drug resistance in typhoid (also called R factors), [114]. As of 2014 some Enterococcus faecium and Pseudomonas aeruginosa strains are resistant to chloramphenicol. Some Veillonella spp. and Staphylococcus capitis strains have also developed resistance to chloramphenicol to varying degrees, [114]. Some other resistance genes beyond cat are known, such as chloramphenicol hydrolase, [115], and chloramphenicol phosphotransferase, [116].

Resistance to chloramphenicol occurs by various mechanisms. The most common is by enzymatic acetylation and inactivation by chloramphenicol acetyltransferases (CATs), [117]. Most CAT genes are located on mobile genetic elements, can be distributed to other bacteria, and often confer resistance to other classes of antimicrobial drugs, [118], [119]. The plasmid-mediated spread of these resistant genes was the cause of the global decrease in S. Typhi susceptibility, [120].

Other mechanisms of resistance occur by decreasing membrane permeability, which prevent uptake of chloramphenicol. Some gram-negative bacteria prevent drug penetration by a change in their outer membrane proteins, [121]. This was demonstrated to be plasmid mediated in P. Aeruginosa and chromosomally mediated in H. influenzae, [122], [123].

Transmembrane efflux pumps have also been shown to confer resistance to both gram-positive and gram-negative organisms, [124], [125]. Lastly, alteration of a 50S ribosomal subunit was found to reduce chloramphenicol binding in Bacillus subtilis, [126].

3 Results and Discussions

3.1 XRD Analysis Results

In the XRD pattern of synthesized c-FD (Figure 3), major peaks were observed at 2θ values 24°, 33°, 35.6°, 49°, 54° and 64° correspond to (111), (121), (210), (212), (103) and (331), respectively. The peak at 2θ=35.6° may be due to α- or γ-phases but the relative intensities of other peaks observed strongly indicated that α-Fe_2O_3 is the dominant phase in the prepared nanocomposite.

*Figure 3 can be found in the Appendix section.

Peaks at 27.54, 33.75, 40.68, 48.6 and 56.89 corresponding to (2111), (222), (134), (440) and (662), respectively, in XRD (Figure 3) clearly indexed the cubic phase of Dy_2O_3. The peak corresponding to 40.68 usually occurs at 43.23 in the XRD of Dy_2O_3.

This shift may be due to the co-precipitation with α-Fe_2O_3 during the synthesis. The nanocomposite is thus a mixture of individual binary oxide phase co-existing in one material.

In the XRD graphs, the absence of sharp peaks corresponding to Fe_2O_3 and Dy_2O_3 represents the coating of biomolecules on the surface of nanocomposite that indicates the amorphous nature of FD. Some unidentified peaks may be due to the formation of a Fe-rich layer at the surface. The XRD reveals the successful synthesis of the Fe_2O_3–Dy_2O_3 nanocomposite using a greener route.

3.2 XPS Analysis Results

The ability of XPS to provide information about the elemental conformation, chemical environmental and oxidation state of the elements present in materials makes it an essential tool. The analysis of XPS survey (Fig. 4a) shows the binding energy corresponds to Dy 3d, O 1s, Fe 2p, C 1s and Si 2p which depicts the chemical composition of FD nanocomposite. Si 2p (Figure 4a), Dy 3d (Figure 4b), Fe 2p (Figure 4c), C 1s (Figure 4d), and O 1s (Figure 4e) XPS patterns were determined.

The XPS spectrum (Figure 4b) shows the characteristic peaks at 1296.7 and 1336.2 nm of Dy 3d shell which validates the existence of Dy^{3+} state. The Dy 3d is distinguished to have a double peak, specifically Dy $3d_{3/2}$ and Dy $3d_{5/2}$ at a BE of ca. 1297 and 1336 eV due to spin–orbit splitting.

*Figure 4 can be found in the Appendix section.

Fig. 4: demonstrates the Fe 2p edge in which it consists of both Fe 2p3/2 and 2p1/2 peaks. The Fe 2p3/2 peak is found to be associated with a satellite peak. The satellite peak of Fe 2p3/2 for Fe2O3 is sighted approximately at 8 eV greater than the main Fe 2p3/2 peak. The peak at 722.6 nm corresponds to 2p1/2 (Figure 4c)

In Figure 4, the peak position of Fe $2p_{3/2}$ has been examined by many researchers and the values are reported between 710.6 and 711. 2 nm. In Figure 4, O 1s edge has been shown, peak at 530.8 nm indicates the oxygen present in Fe_2O_3 and Dy_2O_3 matrix. Similarly, the de-convoluted peaks of C 1s shown in Figure 4 reflect the distinct groups of biomolecules present in nanocomposite. The peak at the binding energy of 283.8 nm indicates the aromatic sp^2 carbon skeleton and peak at 287.3 nm represents the C–O/C–O–C carbon form.

3.3 FESEM and TEM Analyses Results

The shape and morphology of greener methodology assisted FD and c-FD nanocomposites were mapped by FESEM (Figure 5a and 5b) and TEM (Fig. 5c, 5d and 5e) analyses. The surface of the FD nanocomposite consists of irregular boundaries of different shapes (Fig. 5a). The calcination of the sample leads to the removal of extract forms the surface that results in a clear visualization of the shape of the nanocomposite. The c-FD has the rod-like shape, nanorod along with nanoparticles (Fig. 5b).

*Figure 5 can be found in the Appendix section.

Fig. 5: represents the TEM images of the FD and c-FD which depicts the formation of nanorods shaped FD in both the cases. The nano-rice formation can be seen at the edge (blue encircled) (Figure 5c) with other differently sized irregular shaped nanocomposites. After the calcination at 700oC for 1 h, the shape becomes more prominent in calcined form due to the decomposition of organic moieties of clove extract at high temperatures (Figure 5d). The nano-rice can be visualized in c-FD with 55.6 nm width and 176 nm length (Figure 5e). Therefore, the clove extract-mediated synthesis leads to the formation of nanorod-shaped FD-nanocomposites

3.4 VSM Analysis Results

To get insight into the magnetic properties of synthesized samples, we compacted them into pellets that were then cut into suitable sizes. The hysteresis loops of FD and c-FD at room temperature are introduced in Figure 6.

*Figure 6 can be found in the Appendix section.

The curve validates the weak ferromagnetic behavior of the synthesized samples. The bio-synthesized FD has less magnetization saturation value, maybe due to loss of water molecules and OH groups which affects the size and finally the magnetic behavior. The presence of hydroxyl groups is confirmed by FTIR also in FD. Thus, it is proposed that the water and hydroxyl groups on the surface result in spin pairing which influences the magnetic parameter. After the calcination, the magnetization saturation value increases. The reason can be the redistribution of cations in the octahedral and tetrahedral sites.

Characteristic to hematite is the fact that its two magnetic sublattices have equal moment and antiparallel orientation below the Morin temperature, TM=262ºK (- 11.15ºC), for pure hematite, [126]. At temperatures higher than the Morin temperature, the two sublattices are slightly canted, leading to weak ferromagnetism. The magnetic ordering of the weak ferromagnetic type given by uncompensated magnetic

moments is present for a large range of temperatures for the sample milled for 12 h, such that the Morin transition takes place over a temperature range of 256ºK (- 17.15ºC), while for the samples milled for 2 h, 4 h and 8 h the Morin transition is below 70ºK (- 203.15ºC).

The zero-field-cooling-field cooling (ZFC-FC) curves recorded in the temperature interval 5-300ºK (- 268.15-26.85ºC) with an applied magnetic field of 200 Oe. These curves show the way in which the milling time influences the Morin temperature. The 0-h sample presents a hysteresis in temperature described by magnetization as an effect of heating and cooling of the

sample. This hysteresis is associated with the Morin transition, which occurs in the temperature range of 152ºK to 212ºK (- 121.15ºC to – 61.15ºC) for the 0-h sample. After 2-h milling time, this hysteresis occurs at lower temperatures, between 5ºK and 70ºK (- 268.15ºC and – 203.15ºC). A similar behavior is shown by the 4-h milled sample, for which the Morin transition takes place between 6ºK and 60ºK (- 267.15ºC and – 213.15ºC). After 8 h of milling time, the Morin transition occurs between 7ºK and 52ºK (- 266.15ºC and – 221.15ºC), while after 12 h of milling, the Morin transition takes place over a much larger temperature range, between 24ºK and 280ºK (- 249.15ºC and 6.85ºC). This behavior is likely due to a change in spin reorientation in Dy/α-Fe_2O_3 and Fe/Dy_2O_3.

It may also be noted that the values of magnetization are small, as there are not many uncompensated magnetic moments and the antiferromagnetic ordering prevails. The magnetization increases with milling time and this is supported by the ZFC-FC as well as hysteresis loop measurements.

3.5 EDX Analysis Results

The EDX analysis was applied for FD and c-FD nanocomposites (Figure 7). EDX analysis results of FD nanocomposites (Figure 7a) and c-FD (Figure 7b) nanocomposites were determined with elemental compositions.

*Figure 7 can be found in the Appendix section.

3.6 BET Isotherm Analysis Results

The nitrogen adsorption and desorption isotherms in the

presence of liquid nitrogen has been illustrated in Figure 8. The isotherms of synthesized samples were assigned to Type IV isotherm indicating the characteristics of mesoporous material. The results demonstrated that the c-FD (112 m^2/g) (Figure 8b) is more porous than FD (41 m^2/g) (Figure 8a); this can be due to the elimination of organic matter form the surface. Calcination results in an increase in the number of pores that lead to an increase in the specific surface area. Both the samples were evaluated for the adsorption of Chloramphenicol from water.

*Figure 8 can be found in the Appendix section.

3.7 TGA Analysis Results

TGA was done to investigate the thermal behavior of the synthesized samples (Figure 9). The mass loss occurs in three steps: a weight loss of 14.39% in the first step around 100°C because of the evaporation of physiosorbed water and other volatile components on the surface of FD. The second step around 200°C results from the decomposition of the capping agents and biomolecule present on the FD surface (Figure 9).

*Figure 9 can be found in the Appendix section.

The last step weight loss (29.43%) is due to adsorbed oxygen species. After calcination at 700°C, it shows a gradual weight loss upon heating up to 800°C indicating the conversion of unwanted phases like FeO to Fe_2O_3.

3.8 Optical DRS Analysis Results

In order to characterize the optical property changes induced by mechanochemical activation in the dysprosium oxide-hematite system, optical diffuse reflectance spectroscopy (ODRS) measurements were also undertaken in the present study. Figure 10 shows the optical absorption spectra of the dysprosium oxide-hematite equimolar mixture as a function of energy over the UV-VIS-NIR spectral range for all milling times employed.

*Figure 10 can be found in the Appendix section.

For the starting material, hematite has a band gap of 1.9-2.2 eV in the visible region, while the dysprosium oxide exhibits absorption bands primarily in the UV region, with characteristic peaks around 3.35 and 3.49 eV, corresponding to transitions from the ground state to various excited states, [127]. For the ball-milled material, it can be seen that absorbance is considerably enhanced and broadened, an effect we believe to result from the substitution of Dy ions for Fe.

According to Tauc plots, the dependence of $(\alpha E)^2$ as a function of energy (eV) is able to yield the band gap of the compound, [128], [129]. The exponent of 2 was chosen because the 2.2 eV transition in hematite

is indirect. Indeed, it can be observed in Figure 10 that the intercepts give a value of ~ 2.1 eV for the band gap. This value is independent of the milling time employed. Indeed, it can be seen in this figure that there is no absorption below 2.1 eV for all milling times, while above the band gap there is a broad absorption that depends on the milling time employed. These results show that the dysprosium oxide-hematite mixed-oxide nanostructures have semiconductor properties. ODRS analysis results for FD and c-FD were summarized in Table 1.

*Table 1 can be found in the Appendix section.

3.9 Adsorption Studies of Chloram on FD and c-FD Nanocomposites

Adsorption of Chloram onto FD and c-FD nanocomposites at varying operational factors, i.e. the effect of time on adsorption (Figure 11a), ionic strength (Figure 11b), adsorbent dosage (Figure 11c), initial concentration of Chloram (Figure 11d) were researched:

*Figure 11 can be found in the Appendix section.

As the time was increased from 5 min up to 20 and 30 min the Chloram yields increased from 89% and 85% to 99% and 96% at FD and c- FD nanocomposites, respectively (Figure 11a). The maximum Chloram removals were detected as 99% and 96% after 15 min contacting time for FD and c-FD nanocomposites, respectively. Thereafter, no significant enhancement in Chloram removal was observed. The Chloram yields decreased to 95% and 90% after 40 min contacting time FD and c-FD nanocomposites, respectively. Initially, rapid removal of Chloram was due to the presence of an adequate number of available vacant sites and after that it slows down because of competition among the Chloram molecules for the available binding sites and finally equilibrium is attained. At higher Chloram concentrations, the number of adsorption sites will be decreased and the yields therefore decreased, [130], [131].

The adsorptive performance of synthesized adsorbents was investigated at different initial Chloram concentrations of 0.001 mg/l, 0.01, 0.1, 1.0, 2.0, 3.0, 30, 40, 60 and 70 mg/l at pH=7.0 with a contact time of 15 min and adsorbent dose of 2.0 mg/l at room temperature.

The results indicated that adsorptive removal of Chloram yields were 99% and 96% as the Chloram concentration was increased from 0.001 mg/l, 0.01, 0.1, 1.0, 2.0, 3,0, 30 and 40 mg/l (Fig. 11b). Further increase of Chloram concentrations to 50 and 60 mg/l resulted with decreases of it's yields to 90% and 85% for FD and c-FD nanocomposites (Figure 11b).

The Chloram concentrations were chosen according to simulate the surface water (0.001 mg/l, 0.01, 0.1, 1.0 mg/l) and pharmaceutical wastewater (15, 20, 30, 40, 60 and 70 mg/l). Higher removal percentage is due to amplified number of Chloram molecules for the adsorption. But if the initial concentration of Chloram is increased after 40 mg/l, the removal efficiency decreases because at higher Chloram concentration, the number of adsorption sites will be less. The maximum Chloram removal efficiencies were found to be as 99% and 96% with 2 mg/l FD and c-FD nanocomposite concentration after 15 min adsorption time.

The removal efficiency strongly depends upon the adsorbent dose in the adsorption process as it decides the removal efficiency of the adsorbent for the fixed initial concentration of Chloram. In the adsorption of Chloram onto the surface of both synthesized adsorbents, the adsorbent dose was varied from 0.5 mg/l to 3.0 mg/l at fixed Chloram concentration of 40 mg/l. The maximum Chloram removal efficiencies of 99% and 94 % was detected for 2.0 mg/l FD and c-FD nanocomposites concentrations, respectively (Figure 11c). The studies showed that the adsorption efficiency of Chloram antibiotic increases upon increasing the adsorbent dose from 0.5 to up to 2.0 mg/l. This rise in removal efficacy is because several adsorption sites for the adsorption are available due to larger number of adsorption sites leading to greater contact between surface of the adsorbent and Chloram molecules. But when the adsorbent dose was raised to 3 mg/l, the adsorption efficiency of Chloram antibiotic reduced to 95% and 90% for FD and c-FD nanocomposites, respectively. This slightly decrease in adsorption yields is due to partial aggregation of nano-adsorbents in the solution at high nanocomposite concentration, [130].

Therefore, 2.0 mg/l Fe_2O_3–Dy_2O_3 nanocomposite concentration was selected as the optimum dose for the Chloram adsorption process. From the investigation, FD was found to possess better adsorption efficiency towards Chloram as compared to c-FD owing to the greater amount of active adsorption sites appear on the surface of FD resulted from the coating of clove extract. Although, c-FD have slightly lower adsorption efficiency it's advantage is the magnetic separation over biosynthesized FD. Further, the adsorptive performance of synthesized adsorbents was investigated at elevated Fe_2O_3–Dy_2O_3 nanocomposites concentrations. The Chloram adsorption yields decreased at 3 .0 mg/l nanocomposite concentration to 95% and 90% at FD and c-FD nanocomposites (Figure 11c). The higher

removal percentage of Chloram antibiotic at optimized nanocomposite concentration is due to amplified number of Chloram molecules for the adsorption.

The impact of ionic strength of $NaHCO_3$ ions on Chloram adsorption process onto FD and c-FD was tested by varying of ion concentrations from 0.01M up to 1.7 M. In this study, an increase in adsorption efficiency was observed upon increasing the ionic strength from 0.01 to 0.1 M. As the ionic strength was increasing from 0.01 M up to 1.2 M the adsorption efficiencies of Chloram antibiotic increased from 90% and 82% up to 99% and 87%, respectively for FD and c-FD nanocomposites (Figure 11d). This observation may be explained on the basis that the NaHCO3 increases the osmotic pressure of Chloram solution promoting transfer of Chloram into adsorbent pores, thus increasing the adsorption until an ionic stretch concentration of 1.4 M. The adsorption phenomenon is affected by ionic strength through electrostatic forces of interaction between adsorbent and adsorbate ions. These electrostatic interactions have been found to be attractive; therefore, an upturn in ionic strength results in multiplied adsorption, [132]. In this study, an increase in adsorption efficiency was observed upon increasing the ionic strength from 0.01 to 0.1 M.

3.10 Adsorption Kinetics

In an adsorption procedure, it is very crucial to investigate the solute uptake rate and time required to attain the equilibrium at the different initial concentrations of Chloram. To probe, the adsorption kinetics of Chloram on the surface of both FD and c-FD nanocomposites, five separate kinetic models, i.e. pseudo-first-order, pseudo second-order kinetic, intraparticle diffusion, Langmuir and Freundlich adsorption models were employed. Each kinetic model was investigated at distinct primary concentrations of adsorbate and different temperatures, respectively.

In pseudo first order reaction kinetic, log (q_e-q_t) is plotted against t and values of k_1 from which q_e are determined through slope and intercept of regression line, respectively. In pseudo second order, the values of k_2 and q_e are determined from the linear plot of t/q_t vs t.

The linear plots for the second-order kinetics also demonstrated lower R^2 and k_2 rate constants than first-order kinetics at all at initial concentrations of Chloram.

Intra-particle diffusion model explains the diffusion of adsorbate molecules into the adsorbent mainly controls the diffusion process. The solute transfer to the solid occurs in various steps. The initial step involves diffusion of Chloram onto the adsorbent via the liquid film around the adsorbent particles followed by diffusion via pores into internal adsorption sites. Initially, high concentration gradient between the liquid film and the solid surface leads to faster transfer of solute on the solid surface. Therefore, intra-particle diffusion varies with the square root of time. The intraparticle diffusion rate constant (K_{id}) was obtained from the linear plot of q_t vs $t_{1/2}$. The larger value of k_{id} reveals the higher rate of adsorption and the intercept C (mg/g) depicts the boundary layer thickness, i.e. the higher is the value of intercept, larger will be the boundary effect.

The concentration of solute in the solution and surface area available on the adsorbent is the main driving force for the adsorption. Langmuir adsorption isotherm, [133], is expressed as Eq. (7):

$$\frac{C_e}{q_e} = \frac{1}{Q_0 b} + \frac{C_e}{Q_0} (7)$$

where q_e is the quantity of Chloram molecules adsorbed per unit mass of adsorbent (mg/g), Q_o is maximum adsorption amount of adsorbent (mg/g), C_e is the equilibrium concentration of Chloram (mg/l), b is Langmuir constant which measures the energy of adsorption (l/mg).

Based on Eq. (7), the linearity of experimental data can be fitted into the plot of C_e/q_e vs C_e. The high value of regression constant R^2 reflects the monolayer adsorption. Further, Langmuir constant b and Q_o can be obtained from the slope and intercept of linear equations. Further, the Langmuir equation can be analyzed based on a dimensionless equilibrium parameter, R_L, i.e. separation factor given, [134], by Eq. (8):

$$R_L = \frac{1}{1+bC_0} (8)$$

Where, C_0 is the initial solute concentration (mg/l) and b is the Langmuir constant which signifies the type of adsorption. The value of R_L reveals the spontaneity of adsorption process. For irreversible adsorption, R_L=0 and if $0 < R_L < 1$ adsorption is favorable, linear adsorption R_L=1 and for unfavorable adsorption $R_L > 1$. Here, R_L factor for the adsorption of Chloram onto the surface of adsorbents FD and c-FD obtained in the study is in range of $0 < R_L < 1$.

Freundlich adsorption isotherm is centered on multilayer adsorption of solute particles on the heterogeneous adsorbent surface. It assumes that the number of adsorbate molecules enhances considerably with an escalation in concentration. Freundlich isotherm can be represented, [135], by Eq. (9):

$$\log q_e = \log K_f + \frac{1}{n} log C_e (9)$$

Where, q_e is the amount of Chloram molecules adsorbed per unit mass of adsorbent (mg/g), K_f is Freundlich which measures adsorption capacity, C_e is an equilibrium concentration of Chloram (mg/l).

The kinetic constants for all investigated isotherm parameters are reviewed in Tables 2 and Table 3. The lower values of regression and kinetic constants for pseudo first and second order kinetics indicated that the adsorption process was not suitable kinetic to define the Chloram adsorption on FD and c-FD nanocomposites. This suggests the chemisorption as a rate-determining step for Chloram adsorption onto the surface of FD and c-FD nanocomposites. (Tables 2 and 3) This indicates the poor race for the adsorption surface sites in pseudo first and second order reaction kinetics.

*Table 2 can be found in the Appendix section.

*Table 3 can be found in the Appendix section.

From Tables 2 and Table 3 it was found that the Langmuir and Freundlish kinetic constants and R^2 values were lower and the Chloram adsorption cannot be defined with these two kinetics.

As a result, the pseudo-first- and second-order kinetic models cannot identify the liquid adsorption system precisely as these do not explain the diffusion of solute into the adsorbent. Therefore, there is a need to study the diffusion model, i.e. intra-particle diffusion model to explain adsorption process. If the line of linear plot passes through the origin, the adsorption procedure is dominated by intra-particle diffusion. The linear plot of q_t vs $t^{½}$ does follow the trend representing multiple linear sections indicating that adsorption of Chloram on FD and c-FD nanocomposites was affected by more than one process along with intra-particle diffusion. The thermodynamic parameters such as standard enthalpy change (ΔH°, kJ/mol), standard entropy change (ΔS°, kJ/mol.^{o}K) and standard Gibbs free energy (ΔG°, kJ/mol), can be calculated and the parameters was illustrated in Table 4. During Chloram adsorption an exothermic reaction was occurred.

*Table 4 can be found in the Appendix section.

Each section on linearity plot corresponds to different mechanism, i.e. first section represents the external diffusion process involving mass transfer of adsorbate molecules to adsorbent this process that most of Chloram get adsorbed on the external surface of the adsorbent. The second section is film diffusion involving slow diffusion of adsorbate molecules from the boundary layer to adsorbent surface. The third linearity section involves the movement of adsorbate molecules from the surface into the pores of adsorbent. As shown in Tables 2 and Table 3 the Chloram antibiotic adsorption on FD and c-FD can be explained with intraparticle diffusion kinetic with high intraparticle diffusion rate constant (K_{id}) values of 0.982 and 1.98 from 0.0001 mg/l Chloram up to 40 mg/l, respectively with low boundary layer thickness C (0.08 mg/g) with high R^2 values of 0.999.

3.11 Removal Efficiency of Microorganisms

The removal efficiencies of all microorganisms from the surface water with 2 mg/l Fe_2O_3–Dy_2O_3 nanocomposites after15 min were summarized in Table 5.

*Table 5 can be found in the Appendix section.

The maximum 99% removal efficiency was measured for E. Coli microorganisms in surface. The removal efficiencies of microorganisms from surface waters using Fe_2O_3–Dy_2O_3 nanocomposites are ranked as follows: E. coli > Pseudomonas > Enteric viruses > Salmonella, respectively.

The removal mechanisms of the aforementioned microorganisms can be speculated as follows:

Chloramphenicol exerts a bacteriostatic (growth-inhibiting) effect by binding to the 50S subunit of bacterial ribosomes and inhibiting protein synthesis, while the effect of Fe_2O_3-Dy_2O_3 nanocomposites is generally a combination of physical and chemical mechanisms, [111], [119].To understand whether the Fe_2O_3-Dy_2O_3 nanocomposite acts solely as an adsorbent (surface-holding agent) or creates a physiological stress similar to chloramphenicol, the following key differences must be considered, [115]:

Physiological stress mechanisms (Bactericidal effect): Fe_2O_3-Dy_2O_3 nanocomposites not only remove bacteria from the environment through mass transfer, but can also actively trigger the following stress factors; (a) Oxidative stress (ROS): Metal-based nanocomposites (e.g., Ag, ZnO, CuO) cause persistent damage to DNA, proteins, and lipids by generating ROS within cells. This is a multifaceted attack, in contrast to the specific ribosomal target of chloramphenicol. (b) Membrane Disruption: The sharp edges of nanoparticles (especially graphene derivatives) can physically tear the bacterial cell wall or disrupt membrane permeability through electrostatic interactions, leading to cytoplasmic leakage. (c) Ion Release: The release of metal ions (such as Ag^+, Zn^{2+}) from the Fe_2O_3-Dy_2O_3 nanocomposite structure blocks the cell's respiratory

chain and enzyme functions, leading to metabolic collapse, [115].

Adsorption and physical removal: If the Fe_2O_3-Dy_2O_3 nanocomposite works only through adsorption, bacteria can survive but are transferred from the liquid phase to the solid surface; (a) Bacterial wrapping: Especially in composites containing chitosan or graphene oxide, the material can physically trap bacteria, interrupting nutrient exchange. This is an isolation effect rather than a biochemical intervention. (b) Surface adhesion: The high surface area of Fe_2O_3-Dy_2O_3 nanocomposites promotes bacterial adhesion to the surface, separating them from the suspension, [115].

The following methods can be used to verify the effect of the Fe_2O_3-Dy_2O_3 nanocomposite, [120]:

Viability analysis: If only adsorption is present, bacteria attached to the surface can multiply again when transferred to a suitable culture medium. In cases of physiological stress, however, cell death occurs.

Stress markers: Changes in intracellular ROS levels, lipid peroxidation (MDA), or antioxidant enzyme (SOD, CAT) activities are evidence of true physiological stress.

Morphological Examination (SEM/TEM): Electron microscopy images clearly reveal whether the bacteria are merely adhered to the Fe_2O_3-Dy_2O_3 nanocomposite or whether their cell wall has been broken down, [120].

Based on the assumptions given above the microorganism deaths can be attributed the points given below: after adsorption all the microorganisms were cultivated however no alive organisms were detected. Fe_2O_3-Dy_2O_3 nanocomposites cause persistent damage to DNA, proteins, and lipids by generating ROS within cells. The OH^- ion measurements exhibited high OH radical levels (data not shown). SEM and TEM analysis results showed that all microorganisms cell wall has been broken down. At high Chloram (40 mg/l) and low Chloram concentrations (0.001 mg/l) also all the microorganism deaths cannot be attributed to Chloram antibiotic since in the simulated water containing no Chloram antibiotic all the microorganism were death, [136]. It is important to note that the Chloram can be ionized at the surface of Fe_2O_3-Dy_2O_3 nanocomposites, and these charges were stabilized by hydroxyl groups. Chloram is a cationic antibiotic, it can be separated from the Fe_2O_3-Dy_2O_3 nanocomposites. These adsorbent ions can be interacted with the OH groups on it's surface through electrostatic interaction ending with cell deaths.

On the other hand, it is important to note th**at t**he dominant mechanism for the synthesized Fe_2O_3-Dy_2O_3 nanocomposites is surface complexation via electrostatic interactions between cationic Chloram and negatively charged Fe_2O_3-Dy_2O_3 nanocomposites, as confirmed by zeta potential measurements (data not shown). The Chloram molecules ionized at the adsorbent surface, and these charges were stabilized by hydroxyl groups (OH^-), which aided the adsorption process. Since Chloram is a cationic antibiotic, it separates into Fe_2O_3-Dy_2O_3 nanocomposites and Cl^- ions in an aqueous solution. The Fe_2O_3-Dy_2O_3 nanocomposites ion interacts with the OH groups on the surface of Fe_2O_3-Dy_2O_3 nanocomposites through electrostatic interaction.

3.12 Recyclability of FD and c-FD Nano-absorbents

In this study, ethanol was employed for the regeneration

of nano-adsorbents after the treatment. It was noticed that only partially held Chloram could be released from nano-adsorbent surface, the addition of ammonia to methanol favored desorption of Chloram from the applied nano-adsorbents. The operational stability of both nano-adsorbents was revealed by evaluating the Chloram (40 ppm) adsorption after 70 cycle runs. Until 70 cycles the Chloram yields were 99% and 96% at FD and c-FD nanocomposites, respectively **(**Table 5**).**

*Table 5 can be found in the Appendix section.

After 60 cycles the Chloram yields decreased to 88% and 80%. This demonstrates excellent stability and reusability of the nano-adsorbents towards Chloram removal. The removal efficiency of the c-FD was relatively less decreased than the FD due to the robustness of the calcined sample than the biosynthesized sample. The c-FD can be retrieved efficiently, can be put into cycle use, and may become a promising adsorbent in environmental applications.

4 Conclusions

Fe_2O_3–Dy_2O_3 nanocomposite was successfully synthesized and calcination of Fe_2O_3–Dy_2O_3 nanocomposite at 700°C led to magnetic core of nanocomposite. The synthesized nanocomposites were utilized efficiently as adsorbents for the eradication of the antibiotic namely Chloram from aqueous medium at neutral pH (pH=7.0). XRD patterns support the formation of Fe_2O_3–Dy_2O_3 nanocomposite and dysprosium orthoferrite at long milling times. The synthesized nanocomposites exhibit nanorod-shaped morphology as revealed by FESEM analysis. XPS assessment showed the

composition of synthesized Fe_2O_3–Dy_2O_3 nanocomposites.

At optimum condition, adsorption performance of biosynthesized nanocomposite than calcined nano-absorbent.

The detailed kinetic and isotherm modelling showed that the Chloram antibiotic adsorption did not match with the pseudo-second-order and the monolayer pseudo first order adsorption kinetics on the surface of FD and c-FD nanocomposites respectively. With Langmuir and Freundlich adsorption kinetic constants also the Chloram adsorption cannot be defined due to low kinetic constants with low regression coefficients. The removal of Chloram antibiotic in FD and c-FD nanocomposites can be explained with intraparticle diffusion kinetic with high intraparticle diffusion rate constant (K_{id}) values of 0.982 and 1.98 for 0.001 mg/l Chloram up to 40 mg/l, respectively in both nanocomposites, respectively, with low boundary layer thickness C (0.08 mg/g) values and with high R^2 values of 0.999.

The maximum removal percentage of Chloram was found to be 99% for FD and 96% for c-FD nanocomposites at an adsorbent dose of 2 mg/l within 15 min for 40 ppm initial concentration of Chloram at an ionic strength of 1.2 M. The effect of FD and c-FD nanocomposites on the removals of bacterial strains (E. coli, Pseudomonas and Salmonella and viruses (Enteric viruses) were found to be high. The removal efficiencies of microorganisms from surface waters using Fe_2O_3–Dy_2O_3 nanocomposites are ranked as follows: E. coli > Pseudomonas > Enteric viruses > Salmonella, respectively.

The recyclability of the aforementioned nanoadsorbents showed excellent cycling stability and reuse properties**.** The operational stability of both nano-adsorbents was revealed by evaluating the Chloram (40 ppm) adsorption after 60 cycle runs. Until 50 cycles the Chloram yields were 99% and 96% at 2 mg/l FD and c-FD nanocomposites, respectively during 15 min. After 60 cycles the Chloram yields slightly decreased to 88% and 80%. This is very advanantageous for further application of FD nanocomposite in industrial water purification and treatment.

Acknowledgement:
Experimental analyzes in this study were performed at the Laboratories of the Canada Research Center, Ottawa, Canada. The authors would like to thank this body for providing financial support.

References:

[1] K. Kummerer, Antibiotics in the Aquatic Environment—A Review—Part I, Chemosphere, Vol.75, No.4, 2009, pp. 417–434.

[2] M. Bilal, S. Mehmood, T. Rasheed, H. M. Iqbal, Antibiotics Traces in the Aquatic Environment: Persistence and Adverse Environmental Impact, Current Opinion in Environmental Science & Health, Vol.13, 2020, pp. 68-74.

[3] M. Bilal, T. Rasheed, S. Mehmood, H. Tang, L. F. R. Ferreira, R. N. Bharagava, H. M. Iqbal, Mitigation of Environmentally-Related Hazardous Pollutants from Water Matrices Using Nanocomposited Materials—A review, Chemosphere, Vol.253, 2020, 126770.

[4] Z. Li, M. Li, Z. Zhang, P. Li, Y. Zang, X. Liu, Antibiotics in Aquatic Environments of China: A Review and Meta-Analysis, Ecotoxicology and Environmental Safety, Vol.199, 2020, 110668.

[5] W. C. Reygaert, An Overview of the Antimicrobial Resistance Mechanisms of Bacteria, AIMS Microbiology, Vol.4, No.3, 2018, pp. 482-501.

[6] M. Bilal, S. S. Ashraf, D. Barceló, H. M. Iqbal, Biocatalytic Degradation/Redefining "Removal" Fate of Pharmaceutically Active Compounds and Antibiotics in the Aquatic Environment, Science of the Total Environment, Vol.691, 2019, pp. 1190-1211.

[7] E. M. C. Correa, M. F. A. Franco, C. F. González, Advanced Oxidation Processes for the Removal of Antibiotics from Water. An overview, Water, Vol.12, No.1, 2020, pp. 102–107.

[8] F. Tamaddon, A. Nasiri, G. Yazdanpanah, Photocatalytic Degradation of Ciprofloxacin Using CuFe2O4@ Methyl Cellulose Based Magnetic Nanobiocomposite, Methods X, Vol.7, 2020, 100764, pp. 74-81.

[9] F. Yu, S. Sun, S. Han, J. Zheng, J. Ma, Adsorption Removal of Ciprofloxacin by Multi-Walled Carbon Nanotubes with Different Oxygen Contents from Aqueous Solutions, Chemical Engineering Journal, Vol.285, 2016, pp. 588–595.

[10] M. Taheran, M. Naghdi, S. K. Brar, E. J. Knystautas, M. Verma, R. Y. Surampalli, Degradation of Chlortetracycline Using Immobilized Laccase on Polyacrylonitrile Biochar Composite Nanofibrous Membrane, Science of the Total Environment, Vol.605–606, 2017, pp. 315-321.

[11] A. J. Carrasquillo, G. L. Bruland, A. A. MacKay, D. Vasudevan, Sorption of Ciprofloxacin and Oxytetracycline Zwitterions to Soils and Soil Minerals: Influence of Compound Structure, Environmental Science & Technology, Vol.42, No.20, 2008, pp. 7634–7642.

[12] C. J. Wang, Z. H. Li, W. T. Jiang, Adsorption of Ciprofloxacin on 2:1 Dioctahedral Clay Minerals, Applied Clay Science, Vol.53, No.4, 2011, pp. 723-728.

[13] C. Gu, K. G. Karthikeyan, Sorption of the Antimicrobial Ciprofloxacin to Aluminum and Iron Hydrous Oxides, Environmental Science & Technology, Vol.39, No.23, 2005, pp. 9166–9173.

[14] K. W. Goyne, J. Chorover, J. D. Kubicki, A. R. Zimmerman, S. L. Brantley, Sorption of the Antibiotic Ofloxacin to Mesoporous and Nonporous Alumina and Silica, Journal of Colloid and Interface Science, Vol.283, No.1, 2005, pp. 160-170.

[15] T. Rasheed, M. Bilal, A. A. Hassan, F. Nabeel, R. N. Bharagava, L. F. R. Ferreira, H. N. Tran, H. M. Iqbal, Environmental Threatening Concern and Efficient Removal of Pharmaceutically Active Compounds Using Metal-Organic Frameworks as Adsorbents, Environmental Research, Vol.185, 2020, 109436.

[16] D. J. Haldar, P. Duarah, M. K. Purkait, MOFs for the Treatment of Arsenic, Fluoride and Iron Contaminated Drinking Water: A Review, Chemosphere, Vol.251, 2020, 126388.

[17] X.-Y. Liu, K.-X. Wang, J.-S. Chen, Template-Directed Metal Oxides for Electrochemical Energy Storage, Energy Storage Materials, Vol.3, 2016, pp. 1-17.

[18] D. Obermayer, A. M. Balu, A. A. Romero, W. Goessler, R. Luque, C. O. Kappe, Nanocatalysis in Continuous Flow: Supported Iron Oxide Nanoparticles for the Heterogeneous Aerobic Oxidation of Benzyl Alcohol, Green Chemistry, Vol.15, No.6, 2013, pp. 1530-1537.

[19] S. N. Shelke, S. R. Bankar, G. R. Mhaske, S. S. Kadam, D. K. Murade, S. B. Bhorkade, A. K. Rathi, N. Bundaleski, O. M. N. D. Teodoro, R. Zboril, R. S. Varma, M. B. Gawande, Iron Oxide-Supported Copper Oxide Nanoparticles (Nanocat-Fe-CuO): Magnetically Recyclable Catalysts for the Synthesis of Pyrazole Derivatives, 4-Methoxyaniline, and Ullmann-Type Condensation Reactions, ACS Sustainable Chemistry & Engineering, Vol.2, No.7, 2014, pp. 1699–1706.

[20] M. M. Ardakani, M. Maleki, A. Khoshroo, High Performance Electrochemical Sensor Based on Electro Deposited Iron Oxide Nanoparticle: Catecholamine as Analytical Probe, Journal of the Iranian Chemical Society, Vol.14, 2017, pp. 1659–1664.

[21] J. Wu, J. Wang, H. Li, Y. Du, K. Huang, B. Liu, Designed Synthesis of Hematite-Based Nanosorbents for Dye Removal, Journal of Materials Chemistry A, Vol.1, No.34, 2013, pp. 9837–9847.

[22] Y. Lee, U. von Gunten, Oxidative Transformation of Micropollutants During Municipal Wastewater Treatment: Comparison of Kinetic Aspects of Selective (Chlorine, Chlorine Dioxide, Ferrate VI, and Ozone) and Non-Selective Oxidants (Hydroxyl Radical), Water Research, Vol.44, Nol.2, 2010, pp. 555–566.

[23] V. Peings, T. Pigot, P. Baylere, J. M. Sotiropoulos, J. Frayret, Removal of Pharmaceuticals by a Potassium Ferrate(VI) Material: from Practical Implementation to Reactivity Prediction, Environmental Science: Water Research & Technology, Vol.3, No.4, 2017, pp. 699–709.

[24] A. M. H. Félix, C. A. Flores, A. M. Cruz, J. M. Barandiarán, S. S. Guzmán, R. C. Silva, Removal of Tetracycline Pollutants by Adsorption and Magnetic Separation Using Reduced Graphene Oxide Decorated with α-Fe2O3 Nanoparticles, Nanomaterials, Vol.9, No.3, 2019, 313.

[25] Y. Gao, Y. Li, L. Zhang, H. Huang, J. Hu, S. M. Shah, X. Su, Adsorption and Removal of Tetracycline Antibiotics form Aqueous Solution by Graphene Oxide, Journal of Colloid and Interface Science, Vol.368, 2012, pp. 540–546.

[26] X. Li, H. Xu, Z. S. Chen, G. Chen, Biosynthesis of Nanoparticles by Microorganisms and Their Applications, Journal of Nanomaterials, 2011, 270974, pp. 1–16.

[27] J. Singh, T. Dutta, K. H. Kim, M. Rawat, P. Samddar, P. Kumar, Green Synthesis of Metals and their Oxide Nanoparticles: Applications for Environmental Remediation, Journal of Nanobiotechnology, Vol.16, 2018, pp. 84–108.

[28] P. Mondal, M. K. Purkait, Preparation and Characterization of Novel Green Synthesized Iron–Aluminum Nanocomposite and Studying Its Efficiency in Fluoride Removal, Chemosphere, Vol.235, 2019, pp. 391–402.

[29] B. Ahmmad, K. Leonard, M. S. Islam, J. Kurawaki, M. Muruganandham, T. Ohkubo, Y. Kurod, Green Synthesis of Mesoporous Hematite (α-Fe2O3) Nanoparticles and Their Photocatalytic Activity, Advanced Powder Technology, Vol.24, No.1, 2013, pp. 160-167.

[30] H. Su, X. Wang, Y. Sun, D. Xu, L. Li, C. Liu, S. Zeng, D. Sun, Enhancing the Adsorption Capacity of Hematite by Manganese Doping: Facile Synthesis and Its Application in the Removal of Congo Red, Bulletin of the Korean Chemical Society, Vol.38, No.10, 2017, pp. 1155–1162.

[31] P. Mondal, A. Anweshan, M. K. Purkait, Green Synthesis and Environmental Application of Iron-Based Nanomaterials and Nanocomposite: A Review, Chemosphere, Vol.259, 2020, 127509.

[32] X. Liang, S. Zhu, Y. Zhong, J. Zhu, P. Yuan, H. He, J. Zhang, The Remarkable Effect of Vanadium Doping on the Adsorption and Catalytic Activity of Magnetite in the Decolorization of Methylene Blue, Applied Catalysis B: Environmental, Vol.97, No.1–2, 2010, pp. 151-159.

[33] O. M. Lemine, I. Ghiloufi, M. Bououdina, L. Khezami, M. O. Mhmed, A. T. Hassan, Nanocrystalline Ni Doped α-Fe2O3 for Adsorption of Metals from Aqueous Solution, Journal of Alloys and Compounds, Vol.588, 2014, pp. 592-595.

[34] V. Kumar, A. Jain, S. Wadhawan, S. K. Mehta, Synthesis of Biosurfactant-Coated Magnesium Oxide Nanoparticles for Methylene Blue Removal and Selective Pb2+ Sensing, IET Nanobiotechnology, Vol.2, No.3, 2018, pp. 241-253.

[35] M. Vanaja, G. Gnanajobitha, K. Paulkumar, S. R. Kumar, C. Malarkodi, G. Annadurai, Phytosynthesis of Silver Nanoparticles by Cissusquadrangularis: Infuence of Physicochemical Factors, Journal of Nanostructructure in Chemistry, Vol.3, No.1, 2013, pp. 1–8.

[36] K. Gopinath, M. Chinnadurai, N. P. Devi, K. Bhakyaraj, S. Kumaraguru, T. Baranisri, A. Sudha, M. Zeeshan, A. Arumugam, M. Govindarajan, N. S. Alharbi, S. Kadaikunnan, G. Benelli, One-Pot Synthesis of Dysprosium Oxide Nano-Sheets: Antimicrobial Potential and Cyotoxicity on A549 Lung Cancer Cells, Journal of Cluster Science, Vol.28, No.1, 2016, pp. 621–623.

[37] I. M. Deneva, Infrared Spectroscopy Investigation of Metallic Nanoparticles Based on Copper, Cobalt, and Nickel Synthesized Through Borohydride Reduction Method, Journal of Chemical Technology and Metallurgy, Vol.45, No.4, 2010, pp. 351–3789.

[38] M. Balamurugan, S. Saravanan, T. Soga, Synthesis of Iron Oxide Nanoparticles by Using Eucalyptus Globulus Plant Extract, Journal of Surface Science and Nanotechnology, Vol.12, 2011, pp. 363–367.

[39] M. S. Niasari, J. Javidi, Synthesis of Hollow SiO2 Nanoparticles from Dy2O3@SiO2 Core-Shell Nanocomposites via a Recyclable Sonochemical Method, Journal of Cluster Science, Vol.23, 2012, pp. 1019–1028.

[40] K. Z. Kamali, P. Alagarsamy, N. M. Huang, B. H. Ong, H. N. Lim, Hematite Nanoparticles-Modified Electrode Based Electrochemical Sensing Platform for Dopamine, Science World Journal, 2014, 396135, pp. 1–13.

[41] M. R. Nasrabadi, S. M. Pourmortazavi, M. R. Ganjali, P. N. F. Faridbod, M. S. Karim, Preparation of Dysprosium Carbonate and Dysprosium Oxide Efficient Photocatalyst Nanoparticles through Direct Carbonation and Precursor Thermal Decomposition, Journal of Materials Science: Materials in Electronics, Vol.28, 2017, pp. 3325–3336.

[42] M. Chandrasekhar, H. Nagabhushana, K. H. Sudheerkumar, N. Dhananjaya, S. C. Sharma, D. Kavyashree, C. Shivakumara, B. M. Nagabhushana, Comparison of Structural and Luminescence Properties of Dy2O3 Nanopowders Synthesized by Co-Precipitation and Green Combustion Routes, Materials Research Bulletin, Vol.55, 2014, pp. 237–245.

[43] A. Ebrahiminezhad, Z. Hoseinabadi, A. Berenjian, Y. Ghasemi, Green Synthesis and Characterization of Zerovalent Iron Nanoparticles Using Stinging Nettle (Urticadioica) Leaf Extract, Green Processing and Synthesis, Vol.6, No.5, 2017, pp. 469–475.

[44] E. C. Njagi, H. Huang, L. Stafford, H. Genuino, H. M. Galindo, J. B. Collins, G. E.

Hoag, S. L. Suib, Biosynthesis of Iron and Silver Nanoparticles at Room Temperature Using Aqueous Sorghum Bran Extracts, Langmuir, Vol.27, No.1, 2010, pp. 264–271.

[45] M. I. Litter, J. A. Navio, Photocatalytic Properties of Iron-Doped Titania Semiconductors, Journal of Photochemistry and Photobiology, A: Chemistry, Vol.98, 1996, pp. 171–181.

[46] A. V. Fetisov, G. A. Kozhina, S. K. Estemirova, V. B. Fetisov, R. I. Gulyaeva, XPS Study of the Chemical Stability of DyBa2Cu3O6+δ superconductor, Physica C: Superconductivity and its Applications, Vol.508, 2015, pp. 62–68.

[47] D. D. Hawn, B. M. DeKoven, Deconvolution as a Correction for Photoelectron Inelastic Energy Losses in the Core Level XPS Spectra of Iron Oxides, Surface and Interface Analysis, Vol.10, 1987, pp. 63–74.

[48] P. Mills, J. L. Sullivan, A Study of the Core Level Electrons in Iron and Its Three Oxides by Means of X-Ray Photoelectron Spectroscopy, Journal of Physics D: Applied Physics, Vol.16, 1983, pp. 723–732.

[49] M. Muhler, R. Schlögl, G. Ertl, The Nature of the Iron Oxide-Based Catalyst for Dehydrogenation of Ethylbenzene to Styrene 2. Surface Chemistry of the Active Phase, Journal of Catalysis, Vol.138, 1992, pp. 413–444.

[50] C. D. Wagner, D. A. Zatko, R. H. Raymond, Use of the Oxygen KLL Auger Lines in Identification of Surface Chemical States by Electron Spectroscopy for Chemical Analysis, Analytical Chemistry, Vol.52, 1980, pp. 1445–1451.

[51] D. D. Sarma, C. N. R. Rao, XPES Studies of Oxides of Second- and Third-Row Transition Metals Including Rare Earths, Journal of Electron Spectroscopy and Related Phenomena, Vol.20, 1980, pp. 25–45.

[52] S. Mansingh, R. Acharya, S. Martha, K. M. Parida, Pyrochlore Ce2Zr2O7 Decorated Over rGO: A Photocatalyst that Proves to be Efficient Towards the Reduction of 4-Nitrophenol and Degradation of Ciprofloxacin under Visible Light, Physical Chemistry Chemical Physics, Vol.20, 2018, pp. 9872–9885.

[53] S. S. Shankar, A. Ahmad, M. Sastry, Geranium Leaf Assisted Biosynthesis of Silver Nanoparticles, Biotechnology Progress, Vol.19, No.6, 2003, pp. 1627–1631.

[54] J. S. Justus, S. D. D. Roy, A. M. E. Raj, Synthesis and Characterization of Hematite Nanopowders, Materials Research Express, Vol.3, 2016, pp. 105037–105046.

[55] P. Karpagavinayagam, C. Vedhi, Green Synthesis of Iron Oxide Nanoparticles Using Avicennia Marina Flower Extract, Vacuum, Vol.160, 2019, pp. 286–292.

[56] M. V. Mansilla, R. Zysler, D. Fiorani, L. Suber, Annealing Effects on Magnetic Properties of Acicular Hematite Nanoparticles, Physica B: Condensed Matter, Vol.320, 2002, pp. 206–209.

[57] B. Purnama, A. T. Wijayanta, Suharyana, Effect of Calcination Temperature on Structural and Magnetic Properties in Cobalt Ferrite Nano Particles, Journal of King Saud University Science, Vol.31, No.4, 2019, pp. 956–960.

[58] K. S. W. Sing, D. H. Everett, R. A. W. Haul, L. Moscou, R. A. Pierotti, J. Rouquerol, T. Siemieniewska, Reporting Physisorption Data for Gas/Solid Systems with Special Reference to the Determination of Surface Area and Porosity, Pure and Applied Chemistry, Vol. 57, 1985, pp. 603–619.

[59] K. Shimizu, T. Kubo, A. Satsuma, T. Kamachi, K. Yoshizawa, Surface Oxygen Atom as a Cooperative Ligand in Pd Nanoparticle Catalysis for Selective Hydration of Nitriles to Amides in Water: Experimental and Theoretical Studies, ACS Catalysis, Vol.2, 2012, pp. 2467–2474.

[60] A. Meng, J. Xing, Z. Li, Q. Lian, Cr-Doped ZnO Nanoparticles Synthesis, Characterization Adsorption Property and Recyclability, ACS Applied Materials & Interfaces, Vol.7, 2015, pp. 27449–27457.

[61] C. Muthukumaran, V. M. Sivakumar, M. Thirumarimurugan, Adsorption Isotherms and Kinetic Studies of Crystal Violet Dye Removal from Aqueous Solution Using Surfactant Modified Magnetic Nanoadsorbent, Journal of the Taiwan Institute of Chemical Engineers, Vol.63, 2016, pp. 354–362.

[62] S. Yavari, N. M. Mahmodi, P. Teymouri, N. Shahmoradi, A. Maleki, Cobalt Ferrite Nanoparticles: Preparation, Characterization and Anionic Dye Removal Capability, Journal of the Taiwan Institute of Chemical Engineers, Vol.59, 2016, pp. 320–329.

[63] N. Kataria, V. K. Garg, M. Jain, K. Kadirvelu, Preparation, Characterization and

Potential Use of Flower Shaped Zinc Oxide Nanoparticles (ZON) for the Adsorption of Victoria Blue B Dye from Aqueous Solution, Advanced Powder Technology, Vol.27, No.4, 2016, pp. 1180–1188.

[64] W. Weber, J. Morris, Kinetics of Adsorption on Carbon from Solution. Journal of the Sanitary Engineering Division (American Society of Civil Engineers), Vol.89, 1963, pp. 31–60.

[65] W. Konicki, D. Sibera, E. Mijowska, Z. L. Bielun, U. Narkiewicz, Equilibrium and Kinetic Studies on Acid Dye Acid Red 88 Adsorption by Magnetic ZnFe2O4 Spinel Ferrite Nanoparticles, Journal of Colloid and Interface Science, Vol.398, 2013, pp. 152–160.

[66] Y. Tang, H. Guo, L. Xiao, S. Yu, N. Gao, Y. Wang, Synthesis of Reduced Graphene Oxide/Magnetite Composites and Investigation of Their Adsorption Performance of Fluoroquinolone Antibiotics, Colloids and Surfaces A: Physicochemical and Engineering Aspects, Vol.424, 2013, pp. 74–80.

[67] K. H. Edwards, Optometry: Science, Techniques and Clinical Management, Elsevier Health Sciences, p. 102, 2009.

[68] R. Čivljak, M. Giannella, S. Di Bella, N. Petrosillo, Could Chloramphenicol be Used Against ESKAPE Pathogens? A Review of in Vitro Data in the Literature from the 21st Century, Expert Review of Anti-Infective Therapy, Vol.12, No.2, 2014, pp. 249–264.

[69] E. W. Gower, K. Lindsley, S. E. Tulenko, A. A. Nanji, I. Leyngold, P. J. McDonnell, Perioperative Antibiotics for Prevention of Acute Endophthalmitis after Cataract Surgery, The Cochrane Database of Systematic Reviews, Vol.2, 2017, CD006364.

[70] M. Rey, L. Ouedraogo, P. Saliou, L. Perino, Traitement Minute de la Méningite Cérébrospinale Epidémique par Injection Intramusculaire Unique de Chloramphénicol (Suspension Huileuse), Médecine et Maladies Infectieuses (in French), Vol.6, No.4, 1976, pp. 120–124.

[71] S. S. Wali, J. T. Macfarlane, W. R. Weir, P. G. Cleland, P. A. Ball, M. Hassan-King, H. C. Whittle, B. M. Greenwood, Single Injection Treatment of Meningococcal Meningitis. 2. Long-Acting Chloramphenicol, Transactions of the Royal Society of Tropical Medicine and Hygiene, Vol.73, No.6, 1979, pp. 698–702.

[72] J. B. Puddicombe, S. S. Wali, B. M. Greenwood, A Field Trial of a Single Intramuscular Injection of Long-Acting Chloramphenicol in the Treatment of Meningococcal Meningitis, Transactions of the Royal Society of Tropical Medicine and Hygiene, Vol.78, No.3, 1984, pp. 399–403.

[73] B. Pecoul, F. Varaine, M. Keita, G. Soga, A. Djibo, G. Soula, A. Abdou, J. Etienne, M. Rey, Long-Acting Chloramphenicol versus Intravenous Ampicillin for Treatment of Bacterial Meningitis, The Lancet, Vol.338, No.8771, 1991, pp. 862-866.

[74] G. Rozenberg, K. L. S. Dubrovinsky, M. P. Pasternak, O. Naaman, T. Le Bihan, R. Ahuja, High Pressure Structural Studies of Hematite Fe2O3, Physical Review B, Vol.65, 2002, 064112.

[75] W. Bergermayer, H. Schweiger, E. Wimmer, Ab Initio Thermodynamics of Oxide Surfaces: O2 on Fe2O3 (0001), Physical Review B, Vol.69, 2004, 195409.

[76] Y. Zheng, Y. Cheng, Y. Wang, F. Bao, L. Zhou, X. Wei, Y. Zhang, Q. Zheng, Quasicubic-Fe2O3 Nanoparticles with Excellent Catalytic Performance, Journal of Physical Chemistry B, Vol.110, No.7, 2006, pp. 3093-3097.

[77] C. Wu, P. Yin, X. Zhu, C. OuYang, Y. Xie, Synthesis of Hematite (α-Fe2O3) Nanorods: Diameter-Size and Shape Effects on Their Applications in Magnetism, Lithium Ion Battery, and Gas Sensors, Journal of Physical Chemistry B, Vol.110, No.36, 2006, pp.17806-17812.

[78] J. Z. Liu, Morin Transition in Hematite Doped with Iridium Ions, Journal of Magnetism and Magnetic Materials, Vol.54-57, 1986, pp. 901-902.

[79] C. Stroh, F. Tolea, M. Valeanu, L. Diamandescu, T. Xu, M. Sorescu, Ruthenium Oxide-Hematite Magnetic Ceramics Nanostructures, Ceramics International, Part B, Vol.41, No.10, 2015, pp. 14367-14375.

[80] Y. Wu, G. Ran, W. Zhou, D. Lv, C. Ye, N. Li, Q. Shen, P. Yang, Phase Evolution and Microstructure Characteristics of Mo-Based Tb2O3-Dy2O3 Composites Synthesized by Ball Milling and Sintering, Advanced Powder Technology, Vol.29, No.2, 2018, pp. 359-366.

[81] M. Aghazadeh, M. R. Ganjali, Evaluation of Supercapacitive and Magnetic Properties of Fe3O4 Nanoparticles

Electrochemically Doped with Dysprosium Cations: Development of A Novel Iron-Based Electrode, Ceramics International, Vol.44, No.1, 2018, pp. 520-529.

[82] M. M. Baig, M. A. Yousuf, M. F. Warsi, P. O. Agboola, M. Sher, I. Shakir, Surfactant Assisted Synthesis of Rare Earth Dy3+ Substituted MnFe2O4 Nanoparticles, Ceramics International, Vol.45, No.14, 2019, pp. 18014-18022.

[83] G. Padmasree, P. Y. Reddy, C. G. Reddy, Study of Structural, Electrical and Hyperfine Properties of Dy Doped YFeO3, Ceramics International, Part B, Vol.48, No.19, 2022, pp. 28980-28985.

[84] G. Vinod, K. Rajashekhar, J. L. Naik, Dysprosium Doped Cu0.8Cd0.2DyxFe2-xO4 Nano Ferrites: A Combined Impact of Dy3+ on Enhanced Physical, Optical, Magnetic and DC-Electrical Properties, Ceramics International, Vol.49, No.2, 2023, pp. 2829 2851.

[85] S.-J. Huang, L.-Z. Li, X.-H. Wu, J. Tang, R. Wang, Z. Xiong, X. Chang, Effect of Dy Replacing Fe on Microstructure, Electrical Properties, and Magnetic Properties of NiZnCo Ferrite, Ceramics International, Vol.49, No.13, 2023, pp. 22204-22210.

[86] M. Hashim, A. Ahmed, S. A. Ali, S. E. Shirsath, M. M. Ismail, R. Kumar, S. Kumar, S. S. Meena, D. Ravinder, Structural, Optical, Elastic and Magnetic Properties of Ce and Dy Doped Cobalt Ferrites, Journal of Alloys and Compounds, Vol.834, 2020, 155089.

[87] V. Koval, I. Skorvanek, M. Reece, L. Mitoseriu, H. Yan, Effect of Dysprosium Substitution on Crystal Structure and Physical Properties of Multiferroic BiFeO3 Ceramics, Journal of the European Ceramic Society, Vol.34, No.3, 2014, pp. 641-651.

[88] M. A. Almessiere, Y. Slimani, A. V. Trukhanov, A. Baykal, H. Gungunes, E. L. Trukhanova, S. V. Trukhanov, V. G. Kostishin, Strong Correlation Between Dy3+ Concentration, Structure, Magnetic and Microwave Properties of the [Ni0.5Co0.5](DyxFe2-x)O4 Nanosized Ferrites, Journal of Industrial and Engineering Chemistry, Vol.90, 2020, pp. 251-259.

[89] S. S. K. Reddy, N. Raju, C. G. Reddy, P. Y. Reddy, K. R. Reddy, V. R. Reddy, Structural, Electrical, Magnetic and 57Fe Mössbauer Study of Polycrystalline Multiferroic DyFeO3, Journal of Magnetism and Magnetic Materials, Vol.396, 2015, pp. 214-218.

[90] H. Kumar, R. C. Srivastava, J. P. Singh, P. Negi, H. M. Agrawal, D. Das, K. H. Chae, Structural and Magnetic Study of Dysprosium Substituted Cobalt Ferrite Nanoparticles, Journal of Magnetism and Magnetic Materials, Vol.401, 2016, pp. 16-21.

[91] H. Rahimi, A. Ghasemi, R. Mozaffarinia, M. Tavoosi, The Role of Dysprosium on the Structural and Magnetic Properties of (Nd1-xDyx)2Fe14B Nanoparticles, Journal of Magnetism and Magnetic Materials, Vol.424, 2017, pp. 199-206.

[92] P. Kumar, V. Chauhan, P. C. Panday, Role of Dysprosium Doping Concentration on Structural Deformation of Zin Oxide Nanoparticles, Physica B: Condensed Matter, Vol.621, 2021, 413313.

[93] A. D. Korkmaz, Intrinsic Magnetic-Optical Features of Dy3+ Ion Substituted NiCuZn Nanospinel Ferrites via Sonochemical Approach, Physica B: Condensed Matter, Vol.654, 2023, 414741.

[94] G. Garcia-Martinez, L. G. Martinez-Gonzalez, J. I. Escalante-García, A. F. Fuentes, Phase Evolution Induced by Mechanical Milling in Ln2O3:TiO2 Mixtures (Ln=Gd and Dy), Powder Technology, Vol.152, No.1-3, 2005, pp. 72-78.

[95] D. Lv, J. Lu, G. Ran, W. Zhou, M. Wang, Q. Feng, Y. Wu, N. Li, Q. Shen, Ball Milling and Sintering of Neutron Absorber Mo-Based Tb2O3-Dy2O3 Composite and Its Characterization, Powder Technology, Vol.331, 2018, pp. 226-235.

[96] M. Aghazadeh, Mohammad Reza Ganjali, Evaluation of Supercapacitive and Magnetic Properties of Fe3O4 Nanoparticles Electrochemically Doped with Dysprosium Cations: Development of a Novel Iron-Based Electrode, Ceramics International, Vol.44, No.1, 2018, pp. 520-529.

[97] S. Glasser, A. J. Craig, F. Tolea, M. Sofronie, J. A. Aitken, M. Sorescu, Synthesis and Characterization of Gadolinium Oxide-Hematite Magnetic Ceramic Nanostructures, Journal of Minerals and Materials Characterization and Engineering, Vol.11, No.1, 2023, pp. 1-15.

[98] M. Sorescu, F. Tolea, M. Sofronie, V. Kuncser, A. J. Craig, J. A. Aitken, Formation of Skyrmion Phase in the Fe-Co-Si System by

Mechanochemical Activation, Physica B: Condensed Matter, Vol.688, 2024, 416153.

[99] S. Glasser, F. Tolea, A. J. Craig, M. Sofronie, J. A. Aitken, M. Sorescu, Effects of Mechanochemical Activation on the Structural, Magnetic and Optical Properties of Yttrium Iron Garnet-Graphene Nanoparticles, Physica B: Condensed Matter, Vol.650, 2023, 414501.

[100] M. Sorescu, L. Diamandescu, M. Sofronie, C. Pratt, J. Jubeck, Mechanochemical Synthesis and Mössbauer Characterization of Neodymium Oxide Hematite Magnetic Ceramic Nanoparticles: Phase Sequence and Recoilless Fraction, Materials Chemistry and Physics, Vol.277, 2022, 125511.

[101] H. Fan, X. Ma, S. Zhou, J. Huang, Y. Liu, Y. Liu, Highly Efficient Removal of Heavy Metal Ions by Carboxymethyl Cellulose Immobilized Fe3O4 Nanoparticles Prepared via High-Gravity Technology, Carbohydrate Polymers, Vol.213, 2019, pp. 39–49.

[102] L. Zhang, X. Song, X. Liu, L. Yang, F. Pan, J. Lv, Studies on the Removal of Tetracycline by Multi-Walled Carbon Nanotubes, Chemical Engineering Journal, Vol.178, 2011, pp. 26–33.

[103] M. N. Zafar, Q. Dar, F. Nawaz, M. Zafar, M. Iqbal, M. F. Nazar, Effective Adsorptive Removal of Azo Dyes over Spherical ZnO Nanoparticles, Journal of Materials Research and Technology, Vol.8, No.1, 2019, pp. 713–725.

[104] T. S. Anirudhan, J. R. Deep, A. S. Nair, Fabrication of Chemically Modified Graphene Oxide/Nano Hydroxyapatite Composite for Adsorption and Subsequent Photocatalytic Degradation of Aureomycine Hydrochloride, Journal of Industrial and Engineering Chemistry, Vol.47, 2017, pp. 415–430.

[105] P. Kubelka, New Contributions to the Optics of Intensely Light-Scattering Materials, Journal of the Optical Society of America, Vol.38, No.5, 1948, pp. 448-457.

[106] P. Kubelka, F. Munk, Ein Beitrag Zur Optik der Farbanstriche, Zeitschrift für Technische Physik, Vol.12, 1931, pp. 593-601.

[107] W. C. Lipps, E. B. Braun-Howland, T. E. Baxter, Standard Methods for the Examination of Water and Wastewater, (24th. Edition). W. C. Lipps, E. B. Braun-Howland, T. E. Baxter, (editors), American Public Health Association (APHA), American Water Works Association (AWWA), Water Environment Federation (WEF), Elevate Your Standards. American Public Health Association 800 I Street, NW Washington DC: 20001-3770, USA, December 1, 2022; ISBN:9780875532998, 2022.

[108] J. M. Schifano, R. Edifor, J. D. Sharp, M. Ouyang, A. Konkimalla, R. N. Husson, N. A. Woychik, Mycobacterial Toxin MazF-mt6 Inhibits Translation through Cleavage of 23S rRNA at the Ribosomal a Site, Proceedings of the National Academy of Sciences of the United States of America, Vol.110, No.21, 2013, pp. 8501–8506.

[109] The Merck Annual, Chloramphenicol, The Merck Manual, Rahway, NJ, USA: Merck & Co., Inc., Getmany, 2010.

[110] O. Jardetzky, Studies on the Mechanism of Action of Chloramphenicol. I. The Conformation of Chlioramphenicol in Solution, The Journal of Biological Chemistry, Vol.238, No.7, 1963, pp. 2498–2508.

[111] A. D. Wolfe, F. E. Hahn, Mode of Action of Chloramphenicol IX. Effects of Chloramphenicol upon a Ribosomal Amino Acid Polymerization System and Its Binding to Bacterial Ribosome, Biochimica et Biophysica Acta (BBA) - Nucleic Acids and Protein Synthesis, Vol.95, 1965, pp. 146–155.

[112] F. E. Hahn, C. L. Wisseman, H. E. Hopps, Mode of Action of Chloramphenicol. III. Action of Chloramphenicol on Bacterial Energy Metabolism, Journal of Bacteriology, Vol.69, No.2, 1955, pp. 215–223.

[113] J. A. Gil, H. M. Kieser, D. A. Hopwood, Cloning of a Chloramphenicol Acetyltransferase Gene of Streptomyces Acrimycini and Its Expression in Streptomyces and Escherichia Coli, Gene, Vol.38, No.1–3, 1985, pp. 1–8.

[114] Product Data Safety Sheet, Chloramphenicol spectrum of bacterial susceptibility and Resistance, Product Data Safety Sheet, TOKU-E, 2010.

[115] R. H. Mosher, N. P. Ranade, H. Schrempf, L. C. Vining, Chloramphenicol Resistance in Streptomyces: Cloning and Characterization of a Chloramphenicol Hydrolase Gene from Streptomyces Venezuelae, Journal of General Microbiology, Vol.136, No.2, 1990, pp. 293–301.

[116] R. H. Mosher, D. J. Camp, K. Yang, M. P. Brown, W. V. Shaw, L. C. Vining, Inactivation of Chloramphenicol by O-Phosphorylation. A Novel Resistance Mechanism in Streptomyces Venezuelae ISP5230, a Chloramphenicol Producer, The Journal of Biological Chemistry, Vol.270, No.45, 1995, pp. 27000–27006.

[117] F. W. Fraunfelder, F. T. Fraunfelder, Restricting Topical Ocular Chloramphenicol Eye Drop Use in the United States. Did We Overreact?, American Journal of Ophthalmology, Vol.156, No.3, 2013, pp. 420–422.

[118] M. Piraee, R. L. White, L. C. Vining, Biosynthesis of the Dichloroacetyl Component of Chloramphenicol in Streptomyces Venezuelae ISP5230: Genes Required for Halogenation, Microbiology, Vol.150, No. Pt 1, 2004, pp. 85–94.

[119] N. Nathan, T. Borel, A. Djibo, D. Evans, S. Djibo, J. F. Corty, M. Guillerm, K. P. Alberti, L. Pinoges, P. J. Guerin, D. Legros, Ceftriaxone as Effective as Long-Acting Chloramphenicol in Short-Course Treatment of Meningococcal Meningitis during Epidemics: A Randomised Non-Inferiority Study, The Lancet, Vol.366, No.9482, 2005, pp. 308–313.

[120] S. Kaštelan, S. A. Jurica, S. Orešković, T. Župić, M. Herman, A. Gverovic Antunica, I. Marković, I. Bakija, A Survey of Current Prophylactic Treatment for Ophthalmia Neonatorum in Croatia and a Review of International Preventive Practices, Medical Science Monitor, Vol.4, 2018, pp. 8042–8047.

[121] D. M. Boothe, Chloramphenicol and Congeners, Rahway, NJ, USA: Merck & Co., Inc., 2012.

[122] M. Govendir, J. Hanger, J. J. Loader, B. Kimble, J. E. Griffith, L. A. Black, M. B. Krockenberger, D. P. Higgins, Plasma Concentrations of Chloramphenicol after Subcutaneous Administration to Koalas (Phascolarctos Cinereus) with Chlamydiosis, Journal of Veterinary Pharmacology and Therapeutics, Vol.35, No.2, 2012, pp. 147–154.

[123] J. E. Griffith, D. P. Higgins, Diagnosis, Treatment and Outcomes for Koala Chlamydiosis at a Rehabilitation Facility (1995-2005), Australian Veterinary Journal, Vol.90, No.11, 2012, pp. 457–463.

[124] L. A. Black, A. J. McLachlan, J. E. Griffith, D. P. Higgins, A. Gillett, M. B. Krockenberger, M. Govendir, Pharmacokinetics of Chloramphenicol Following Administration of Intravenous and Subcutaneous Chloramphenicol Sodium Succinate, and Subcutaneous Chloramphenicol, to Koalas (Phascolarctos Cinereus), Journal of Veterinary Pharmacology and Therapeutics, Vol.36, No.5, 2013, pp. 478–485.

[125] J. He, N. Magarvey, M. Piraee, L. C. Vining, The Gene Cluster for Chloramphenicol Biosynthesis in Streptomyces Venezuelae ISP5230 Includes Novel Shikimate Pathway Homologues and a Monomodular Non-Ribosomal Peptide Synthetase Gene, Microbiology, Vol.147, No.Pt 10, 2001, pp. 2817–2829.

[126] L. T. Fernández-Martínez, C. Borsetto, J. P. Gomez-Escribano, M. J. Bibb, M. M. Al-Bassam, G. Chandra, M. J. Bibb, New Insights into Chloramphenicol Biosynthesis in Streptomyces Venezuelae ATCC 10712, Antimicrobial Agents and Chemotherapy, Vol.58, No.12, 2014, pp. 7441–7450.

[127] O. B. Aljewaw, M. K. A. Karim, H. M. Kamari, M. H. M. Zaid, N. M. Noor, I. N. C. Isa, M. H. A. Mhareb, Impact of Dy2O3 Substitution on the Physical, Tructural and Optical Properties of Lithium-Aluminium-Borate Glass System, Applied Sciences, Vol.10, No.22, 2020, 10228183.

[128] J. Tauc, R. Grigorovici, A. Vancu, Optical Properties and Electronic Structure of Amorphous Germanium, Physica Status Solidi, Vol.15, No.2, 1966, pp. 627-637.

[129] P. Mallick, Dash, B.N., X-ray Diffraction and UV-Visible Characterizations of -Fe2O3 Nanoparticles Annealed at Different Temperature, Nanoscience and Nanotechnology, Vol.3, 2013, pp. 130-134.

[130] C. Muthukumaran, V. M. Sivakumar, M. Thirumarimurugan, Adsorption Isotherms and Kinetic Studies of Crystal Violet Dye Removal from Aqueous Solution Using Surfactant Modified Magnetic Nanoadsorbent, Journal of the Taiwan Institute of Chemical Engineers, Vol.63, 2016, pp. 354–362.

[131] S. Yavari, N. M. Mahmodi, P. Teymouri, N. Shahmoradi, A. Maleki, Cobalt Ferrite Nanoparticles: Preparation, Characterization and Anionic Dye Removal

Capability, Journal of the Taiwan Institute of Chemical Engineers, Vol.59, 2016, pp. 320–329.

[132] F. Yu, S. Sun, S. Han, J. Zheng, J. Mab, Adsorption Removal of Ciprofloxacin by Multi-Walled Carbon Nanotubes with Different Oxygen Contents from Aqueous Solutions, Chemical Engineering Journal, Vol.285, 2016, pp. 588–595.

[133] P. Tabrizian, W. Ma, A. Bakr, M. S. Rahaman, pH-Sensitive and Magnetically Separable Fe/Cu Bimetallic Nanoparticles Supported by Graphene Oxide (GO) for High-Efficiency Removal of Tetracyclines, Journal of Colloid and Interface Science, Vol.534, 2019, pp. 549–562.

[134] S. T. D. Glu, S. S. Bayazit, O. Kerkez, B. G. Alhogbid, M. A. Salam, Removal of Ciprofloxacin from Aqueous Solution Using Humic Acid and Levulinic Acid Coated Fe3O4 Nanoparticles, Chemical Engineering Research and Design, Vol.123, 2017, pp. 259–267.

[135] Z. Cao, X. Liu, J. Xu, J. Zhang, Y. Yang, J. Zhou, X. Xu, G. V. Lowry, Removal of Antibiotic Florfenicol by Sulfide-Modified Nanoscale Zero-Valent Iron, Environmental Science & Technology, Vol.51, No.19, 2017, pp. 11269–11277.

[136] M. Arakha, S. Pal, D. Samantarrai, Antimicrobial Activity of Iron Oxide Nanoparticle upon Modulation of Nanoparticle-Bacteria Interface, Scientific Reports, Vol.5, 2015, 14813.

Contribution of Individual Authors to the Creation of a Scientific Article (Ghostwriting Policy)

Prof. Dr. Delia Teresa Sponza and Post-Dr. Rukiye Öztekin took an active role in every stage of the preparation of this article.

The authors equally contributed in the present research, at all stages from the formulation of the problem to the final findings and solution.

Sources of Funding for Research Presented in a Scientific Article or Scientific Article Itself

The experimental phases of this research study were conducted at the National Research Council (NRC) of Canada, Research Centers, Ontario, Canada. The authors would like to thank this body for providing financial support.

Conflict of Interest

The authors have no conflicts of interest to declare that are relevant to the content of this article.

APPENDIX

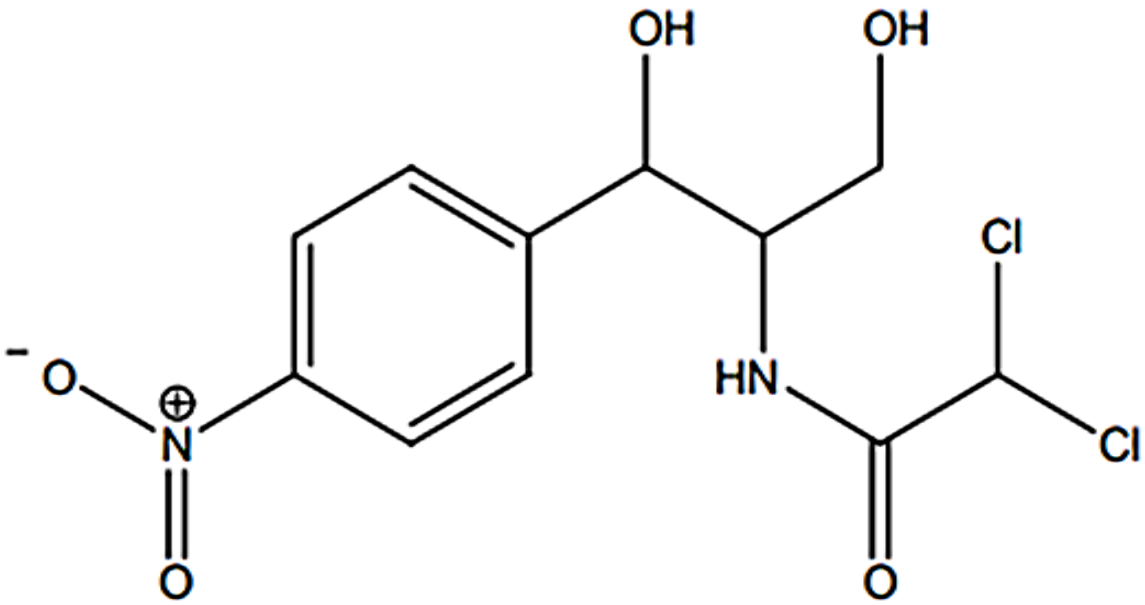

Fig. 1: Structure of chloramphenicol (MW=323.13 g/mol)

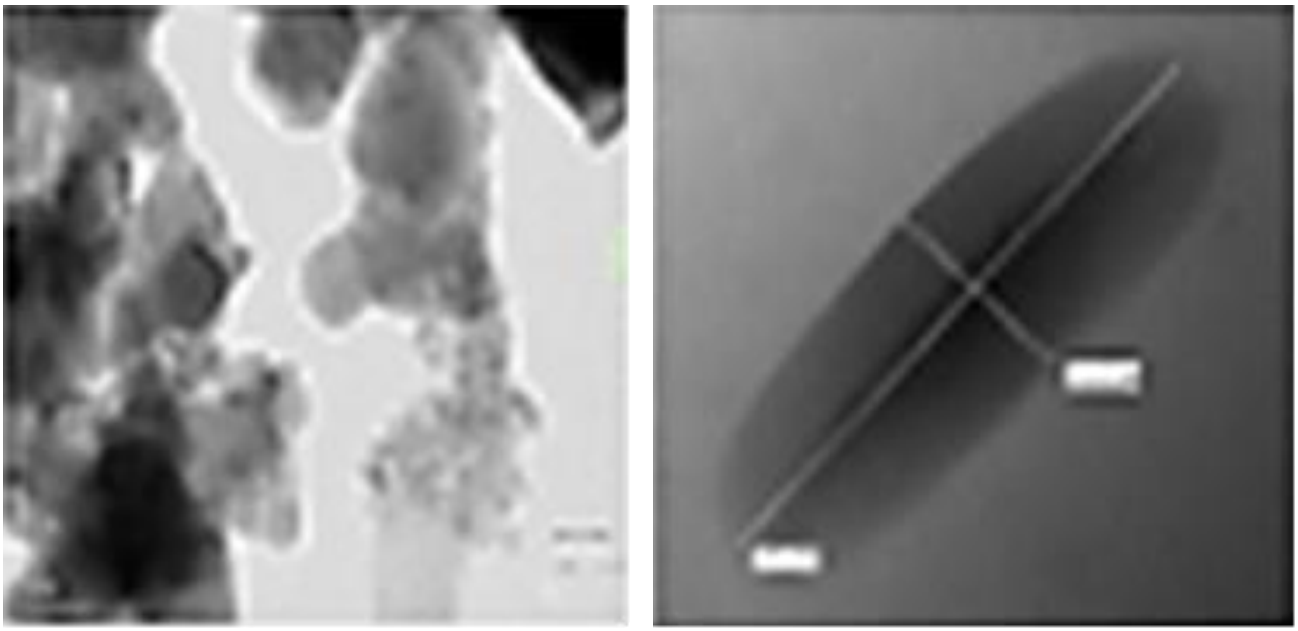

(a) **(b)**

Fig. 2: FESEM images of (a) FD nanocomposites, (b) c-FD nanocomposites, respectively

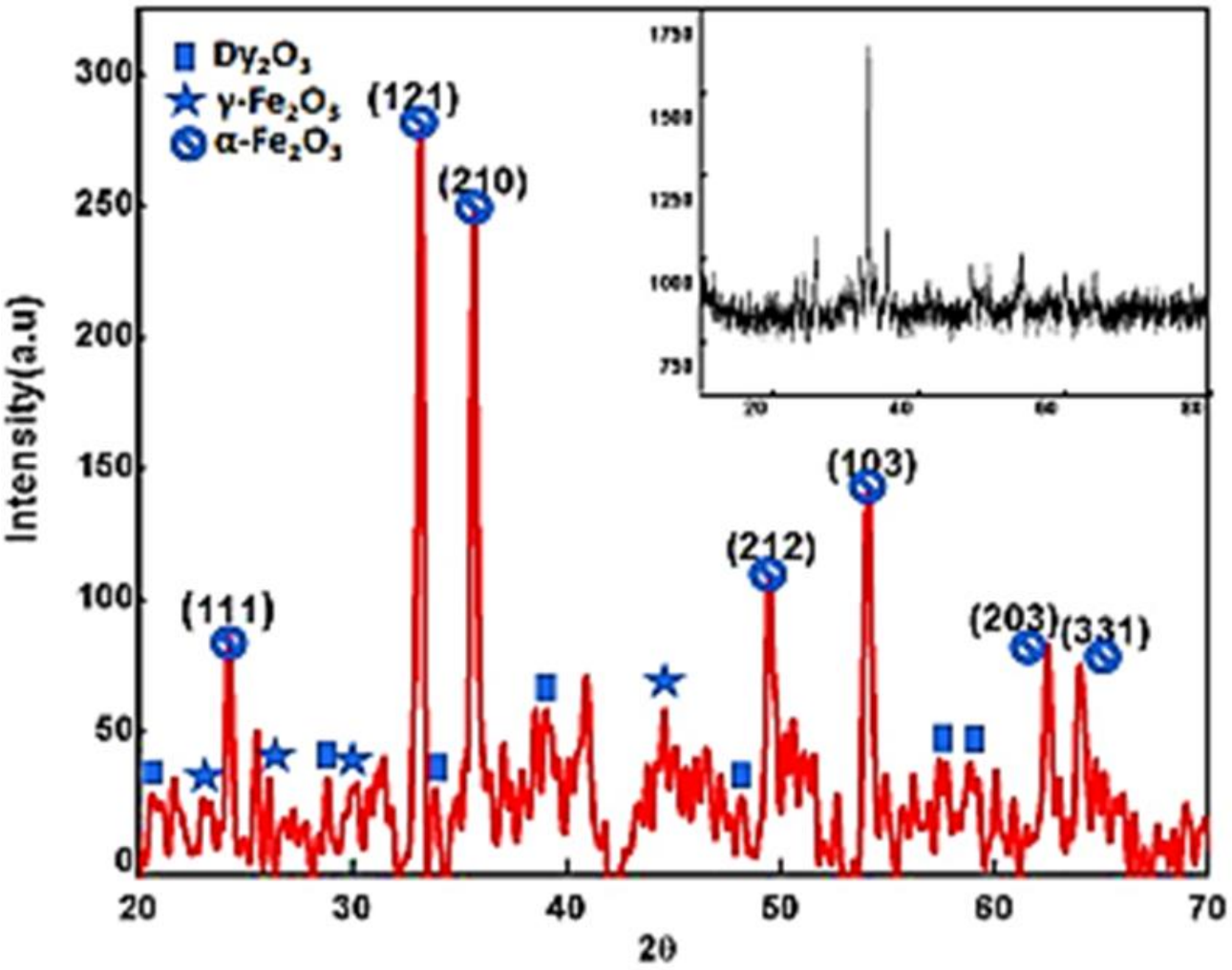

Fig. 3: XRD pattern of hematite dysprosium oxide (Fe2O3–Dy2O3) nanocomposites

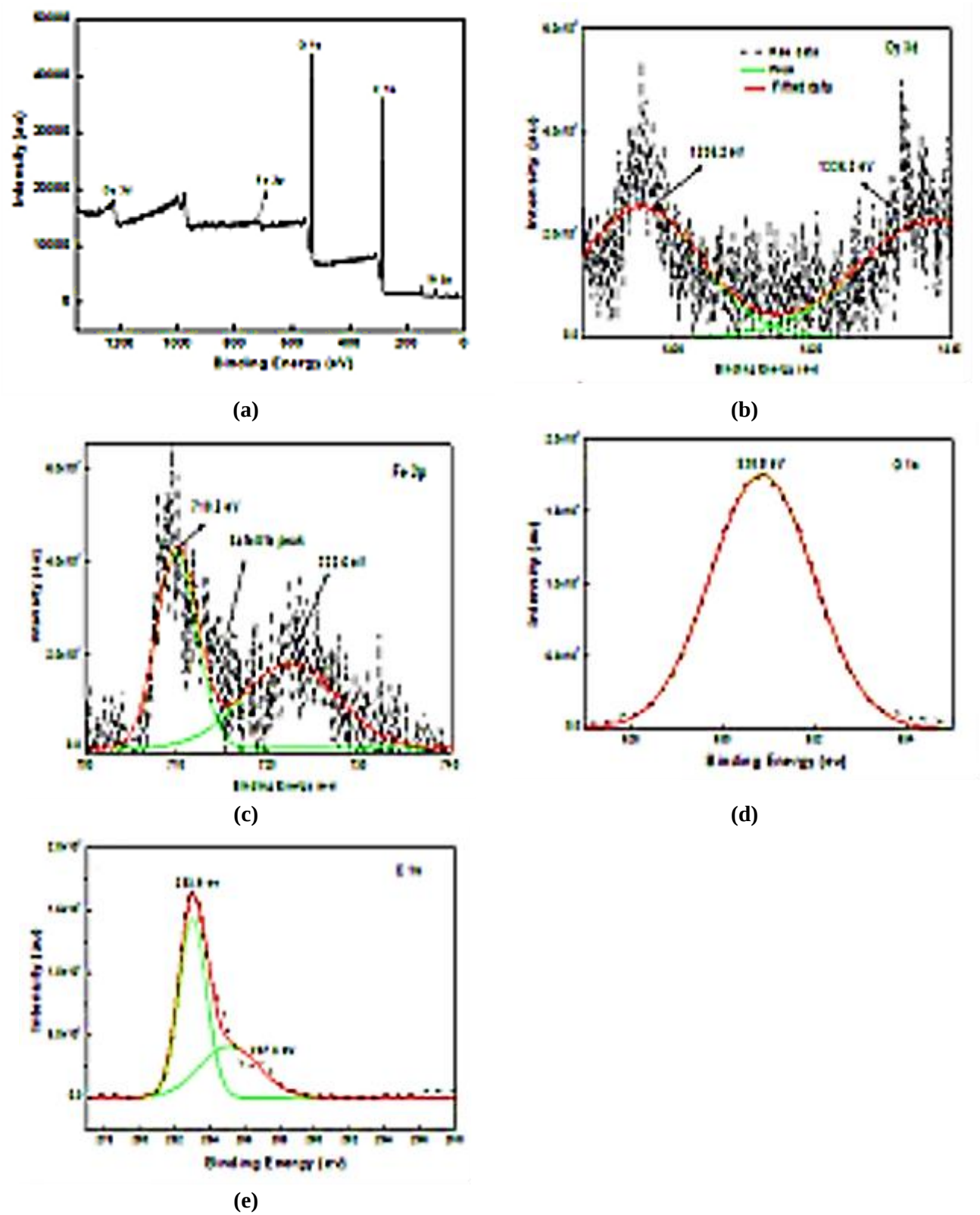

Fig. 4: XPS patterns of (a) Si 2p, (b) Dy 3d, (c) Fe 2p, (d) C 1s, and (e) O 1s, respectively

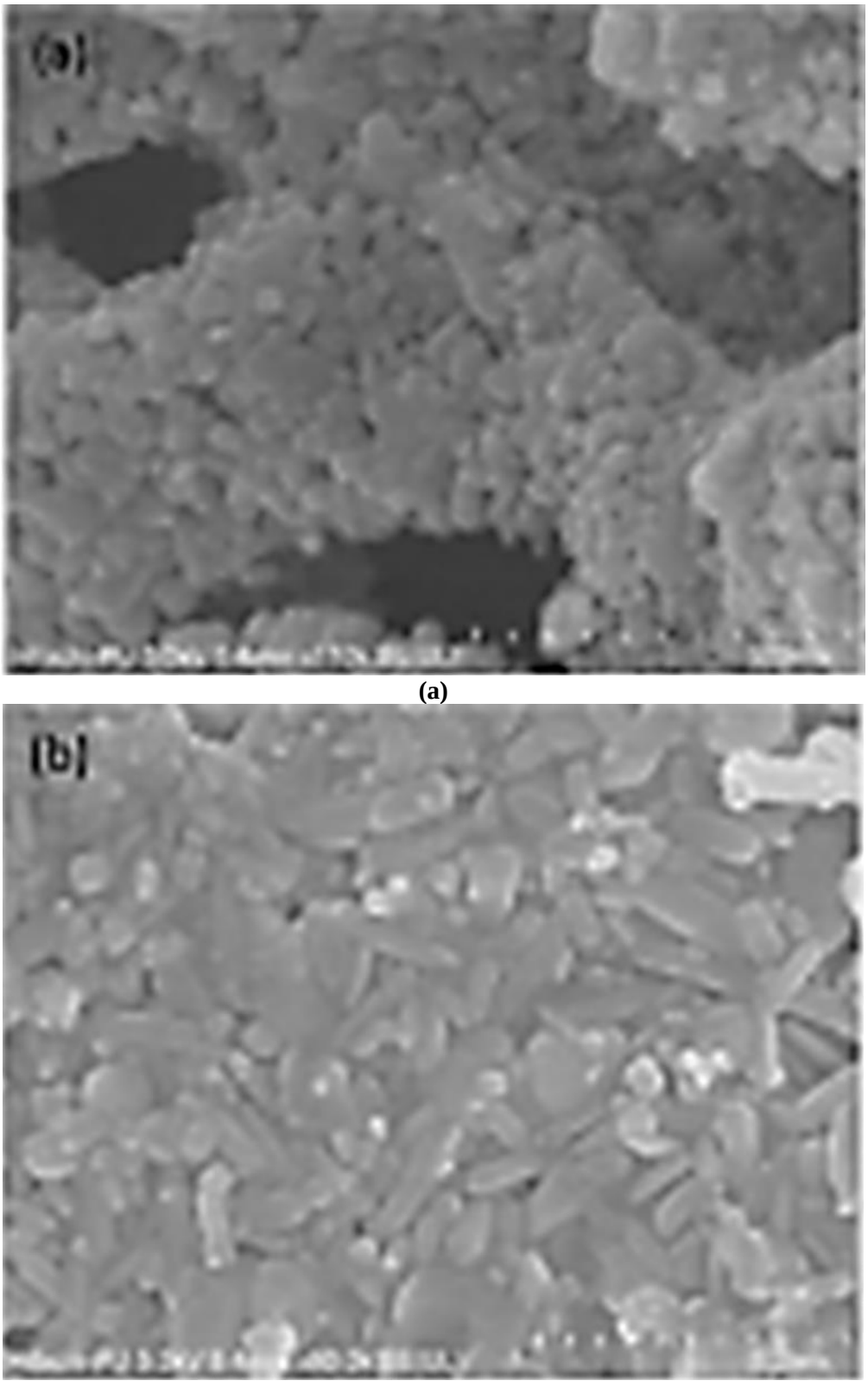

Fig. 5: FESEM images of (a) the surface of the FD nanocomposite consists of irregular boundaries of different shapes, (b) the c-FD nanocomposite has the rod-like shape, nanorod along with nanoparticles, respectively. (FESEM images size: 100 nm)

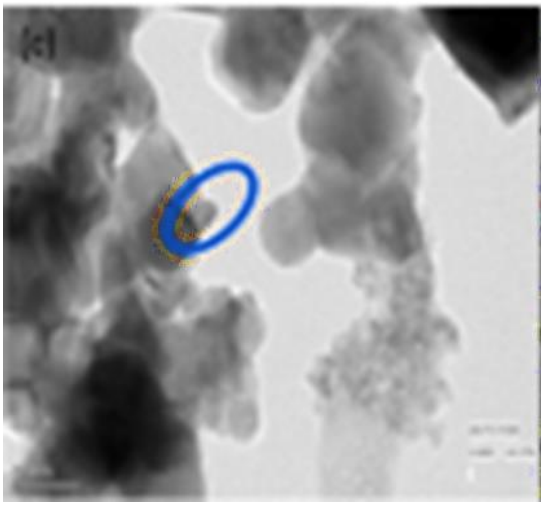

(c)

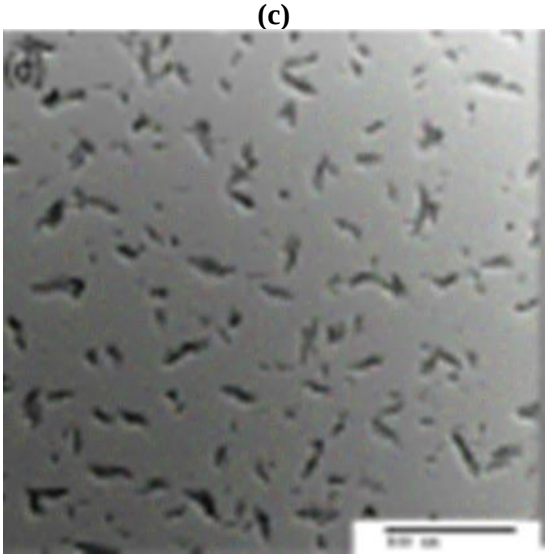

(d)

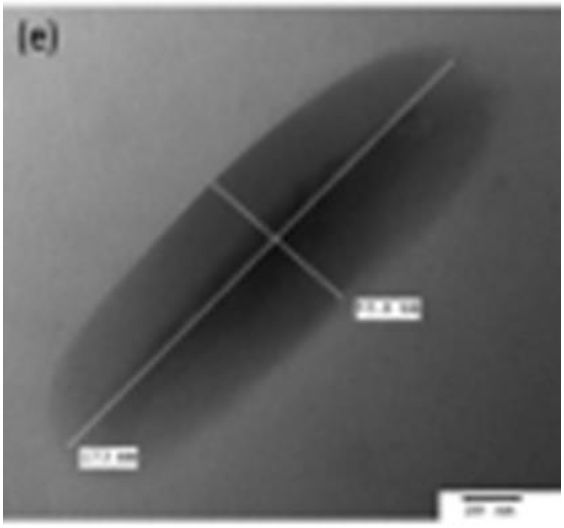

(e)

Fig. 5: TEM images of (c) the nano-rice formation can be seen at the edge (blue encircled), (d) after the calcination at 700oC for 1 h, the shape becomes more prominent in calcined form due to the decomposition of organic moieties of clove extract at high temperatures, and (e) the nano-rice can be visualized in c-FD with 55.6 nm width and 176 nm length, respectively. (TEM images size: 100 nm)

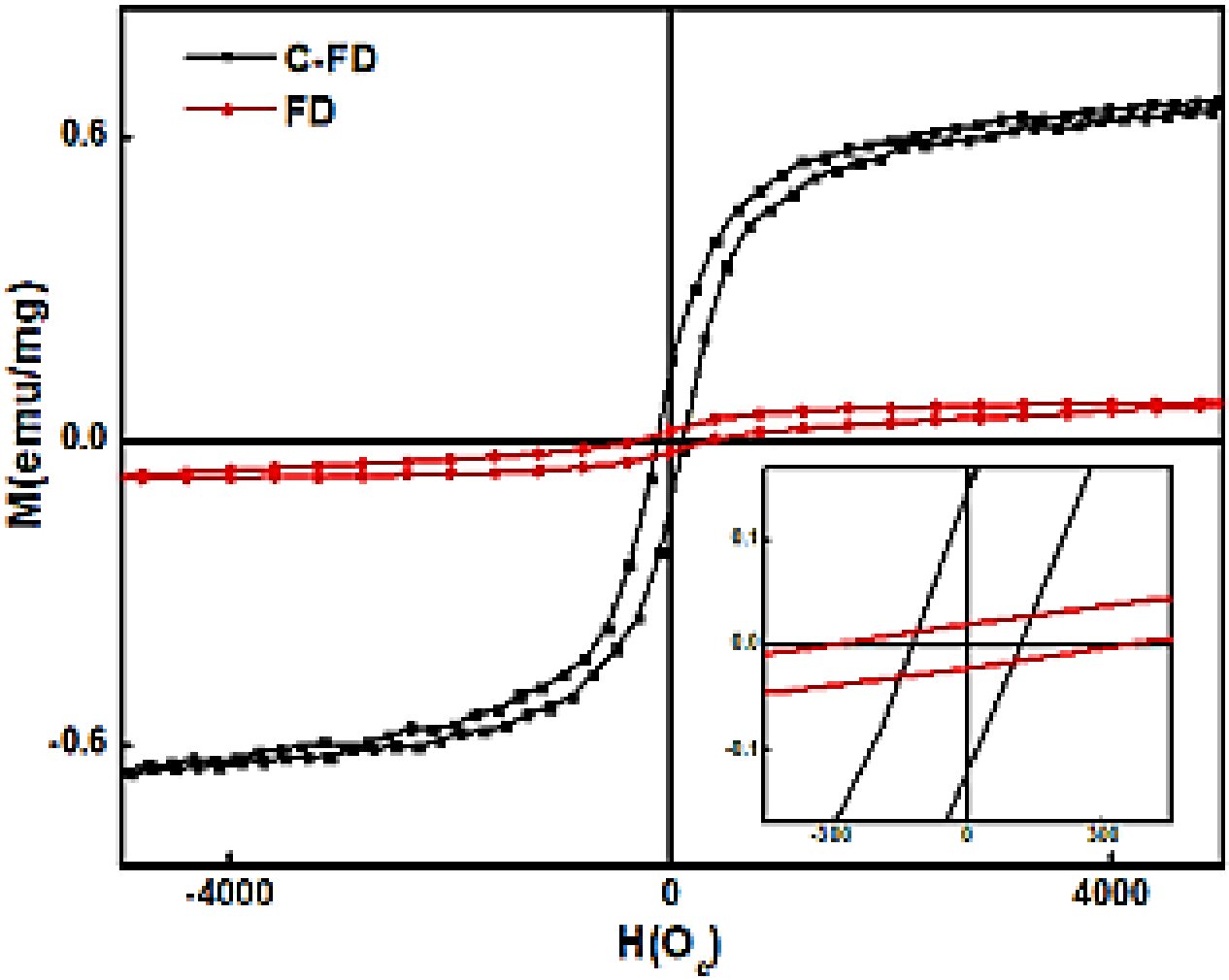

Fig. 6: The magnetic properties of synthesized samples, the hysteresis loops of FD (red line) and c-FD (black line) at room temperature are observed in VSM

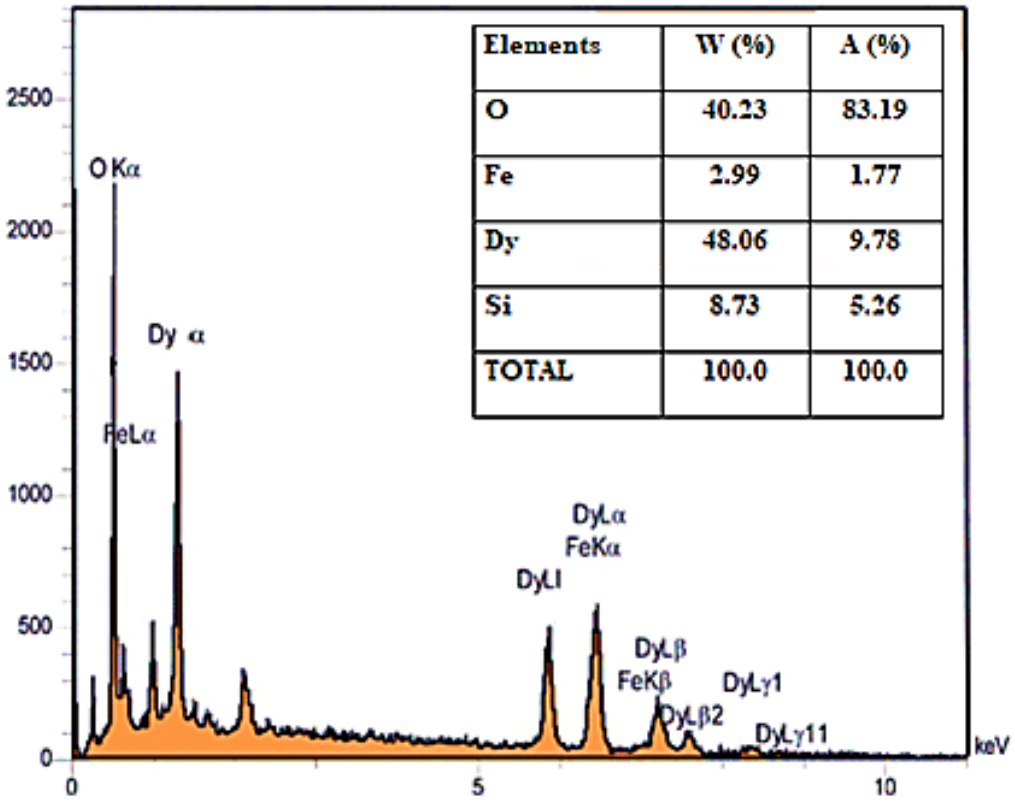

Elements	W (%)	A (%)
O	40.23	83.19
Fe	2.99	1.77
Dy	48.06	9.78
Si	8.73	5.26
TOTAL	100.0	100.0

(a)

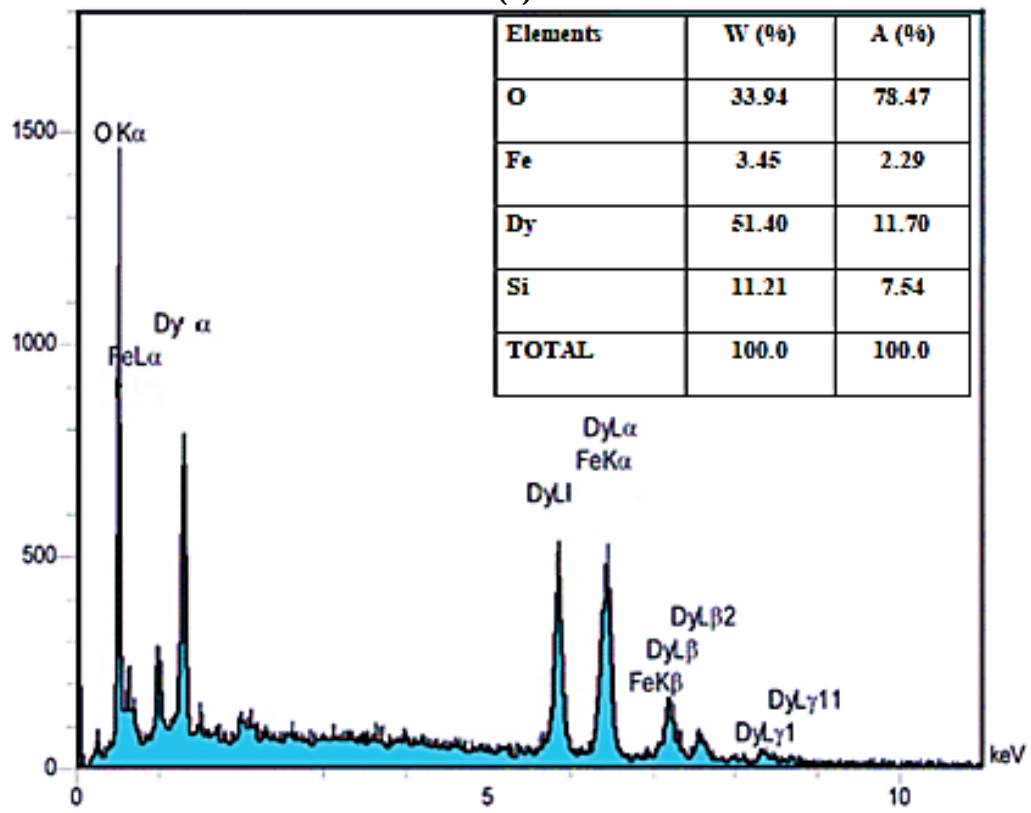

Elements	W (%)	A (%)
O	33.94	78.47
Fe	3.45	2.29
Dy	51.40	11.70
Si	11.21	7.54
TOTAL	100.0	100.0

(b)

Fig. 7: EDX patterns of (a) FD nanocomposite and (b) c-FD nanocomposite, respectively

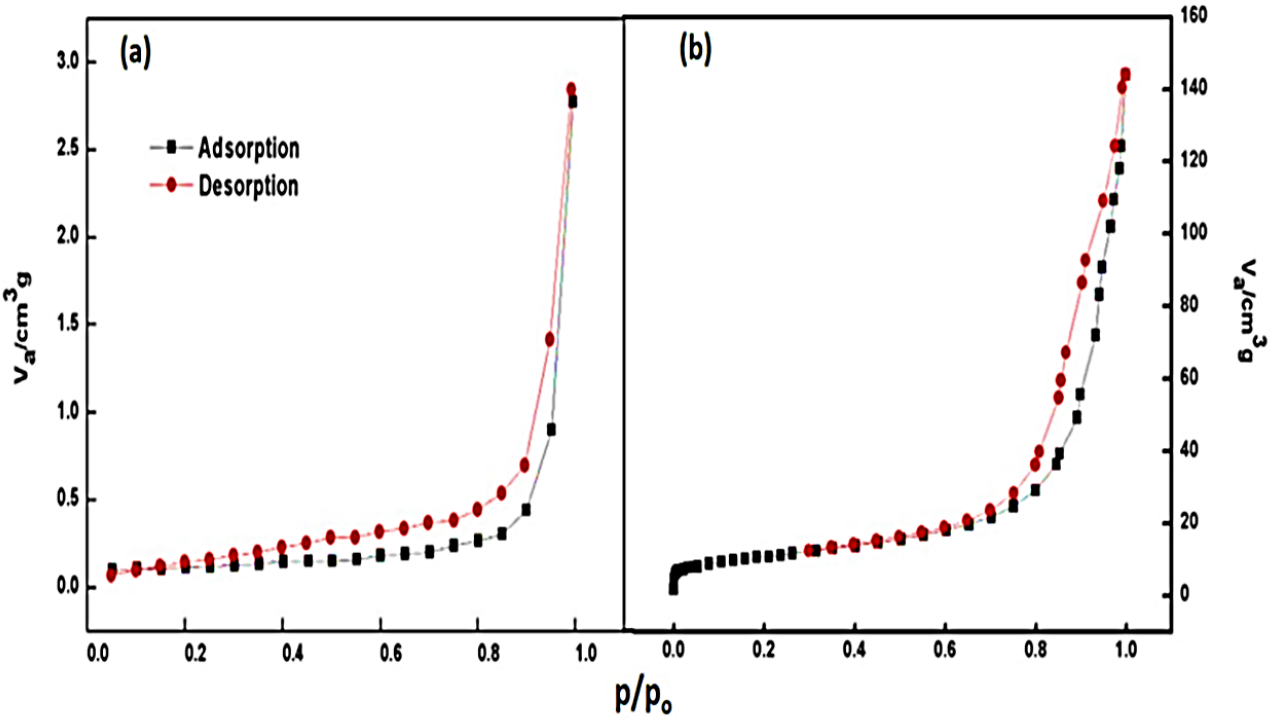

Fig. 8: The nitrogen adsorption and desorption isotherms in the presence of liquid nitrogen has been illustrated in BET for (a) FD nanocomposite, and (b) c-FD nanocomposite, respectively

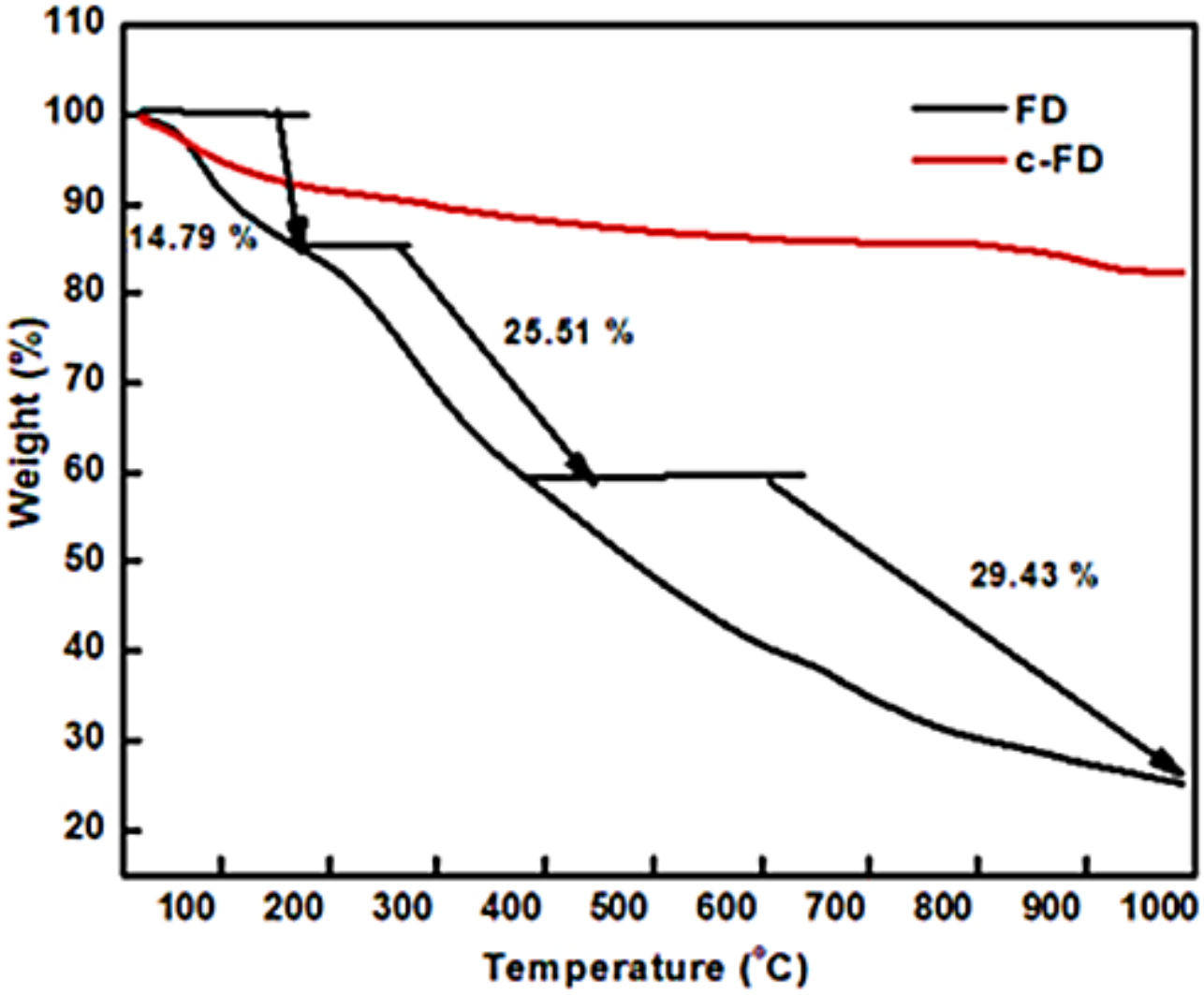

Fig. 9: TGA analysis results of FD (red line) and c-FD (black line) nanocomposites, respectively

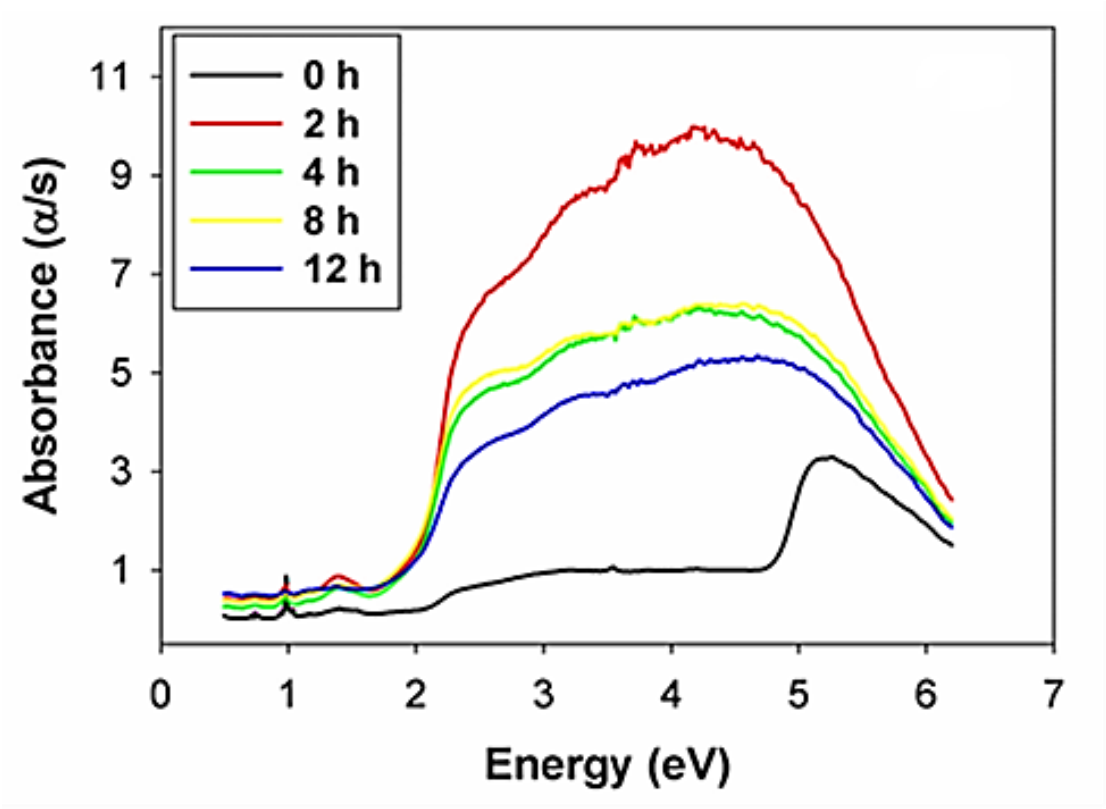

(a)

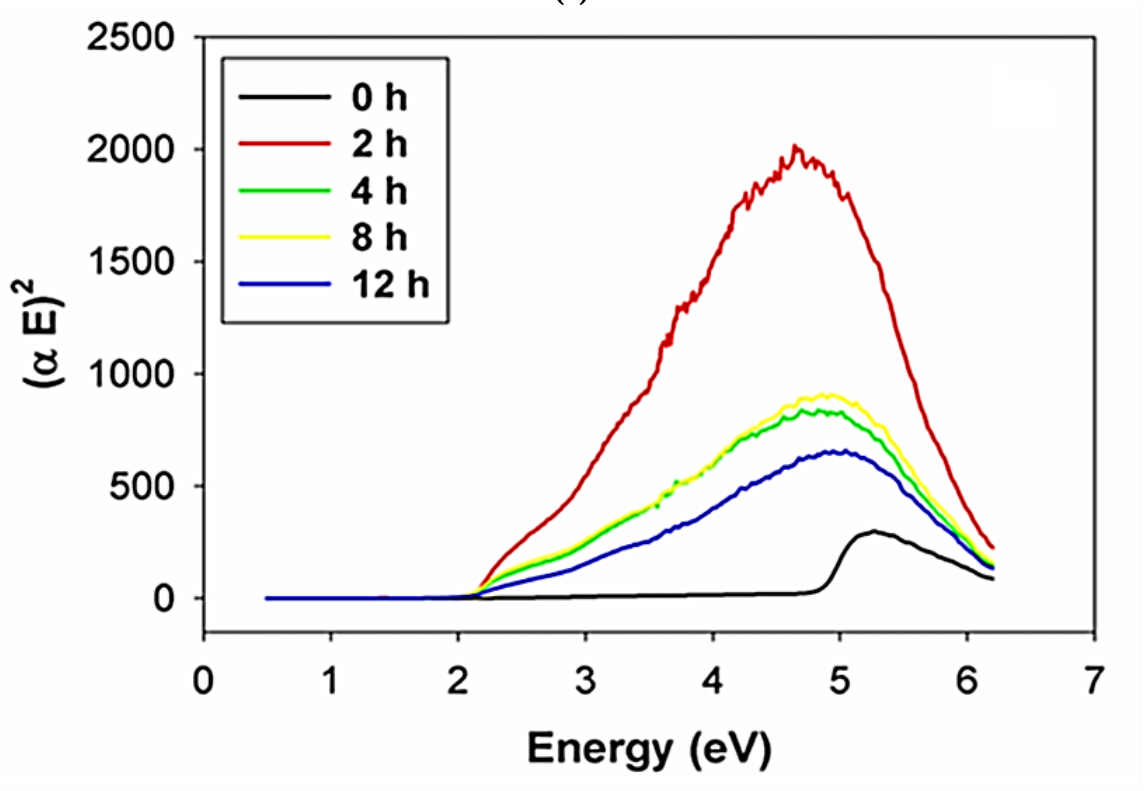

(b)

Fig. 10: ODRS spectra of (a) 0.1 M Fe2O3-Dy2O3 nanocomposites and (b) 0.5 M Fe2O3-Dy2O3 nanocomposites of 0 h, 2 h, 4 h, 8 h and 12 h, respectively

Table 1. ODRS analysis results for Fe_2O_3, Dy_2O_3, FD and c-FD nanocomposites

Time (hours)	**Fe_2O_3 Band gap Energy (Eg) (eV)**	**Dy_2O_3 Band gap Energy (Eg) /eV)**	**FD Band gap Energy (Eg) (eV)**	**c-FD Band gap Energy (Eg) (eV)**
0	1.9	3.35	3.40	3.50
2	2.0	3.40	3.42	3.60
4	2.1	3.44	3.51	3.65
8	2.1	3.47	3.54	3.67
12	2.2	3.49	3.60	3.69

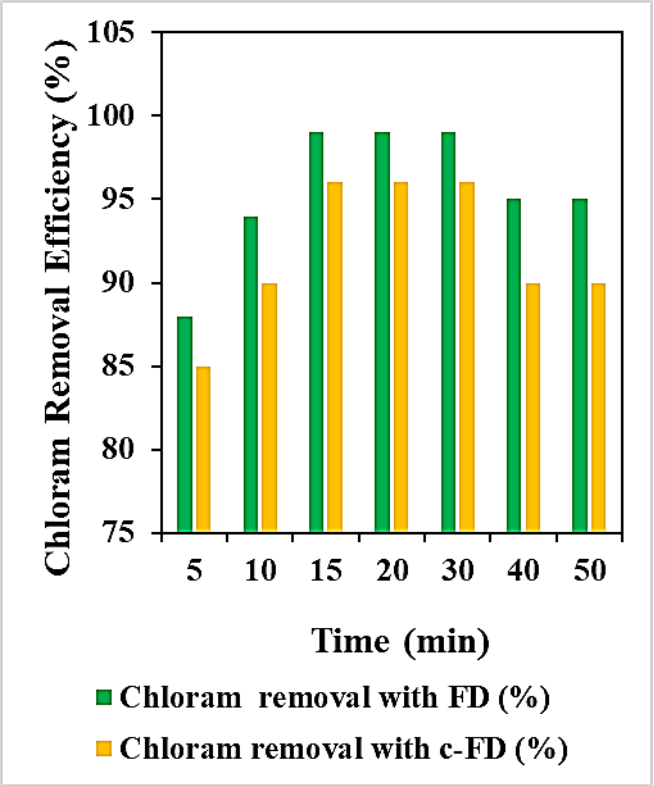

(a)

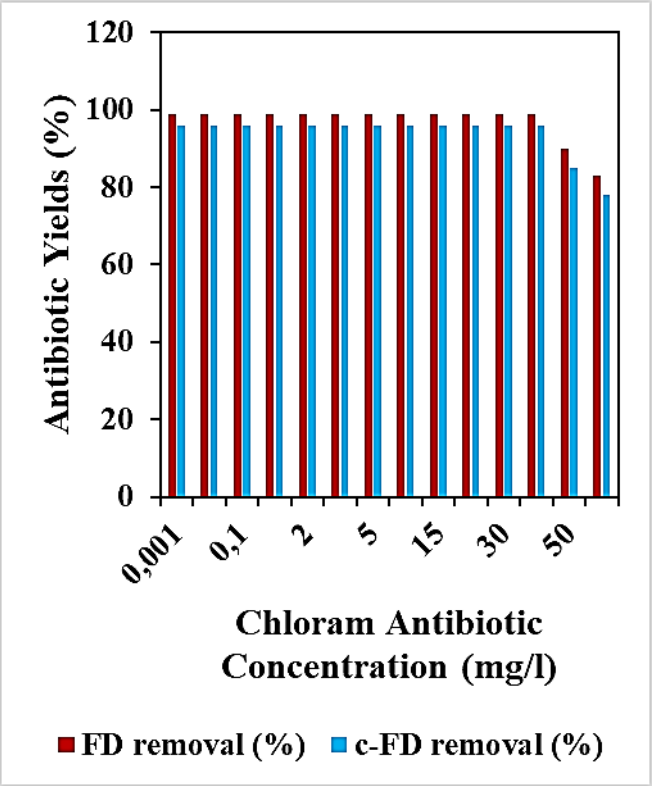

(b)

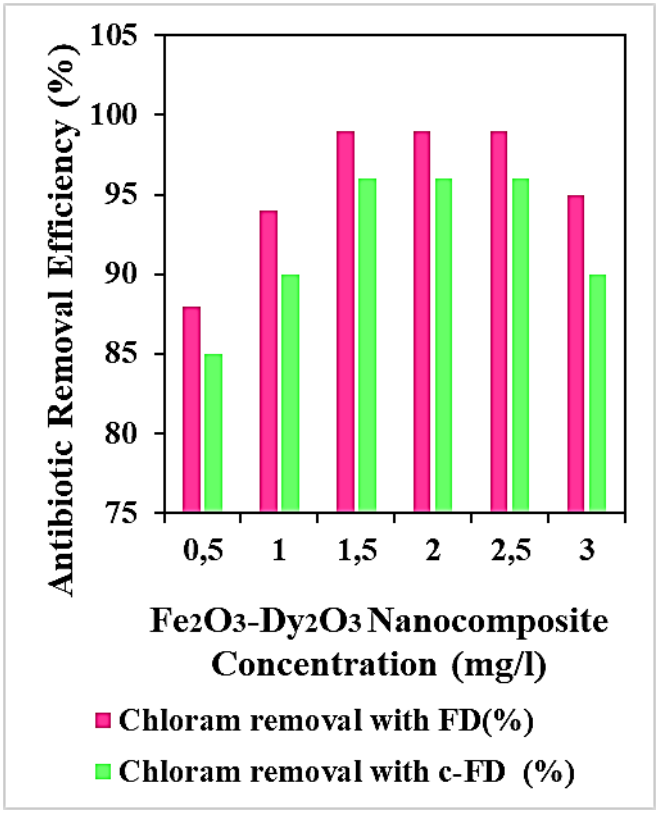

(c)

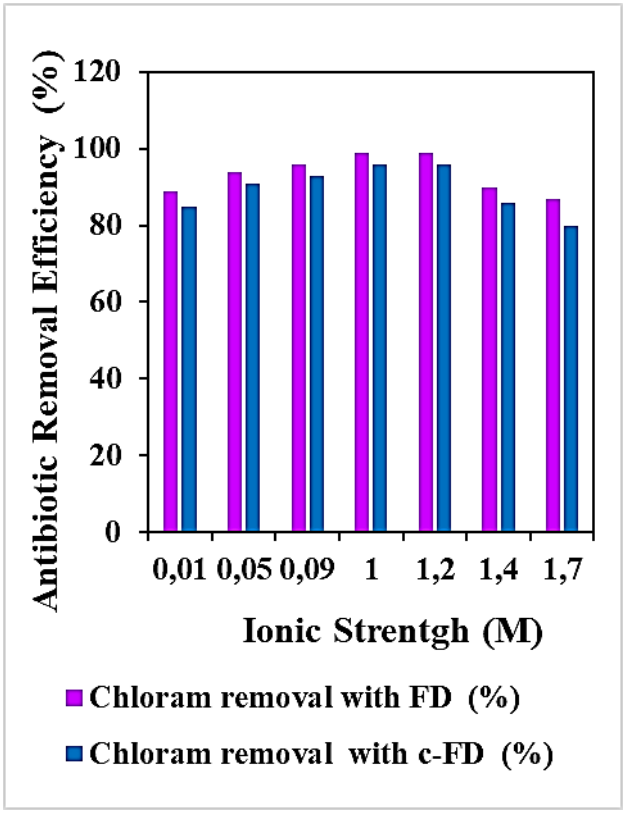

(d)

Fig. 11: (a) Variation of Chloram yields versus time and nanocomposite types, (b) Variation of Chloram yields versus Chloram antibiotic concentration and nanocomposite types, (c) Variation of Chloram yields versus Fe2O3–Dy2O3 and c-synthesized Fe2O3–Dy2O3 nanocomposite concentrations and nanocomposite types, and (d) Variation of Chloram yields versus increasing ionic strength concentrations, respectively

Table 2. Kinetic parameters at different Chloram concentrations for the adsorption of Chloram on the surface of FD

Initial chloram conc. (mg/l)	Pseudo 1st order			Pseudo 2nd order			Intraparticle diffusion			Langmuir adsorption isotherm			Freundlich adsorption isotherm		
	K_1 (min^{-1})	q_e (mg/g)	R^2	K_2 (min^{-1})	q_e (mg/g)	R^2	K_{id}	c (mg/g)	R^2	q_{max} (mg/g)	K_L (l/mg)	R^2	K_F (mg/g)(l/mg)$^{1/n}$	1/n	R^2
0.001							0.982	0.003	0.999	3.10	0.048	0.780	0.037	0.1	0.694
0.01	0.055	2.58	0.702	0.021	1.94	0.787	0.998	0.004	0.994	3.12	0.051	0.797	0.042	0.1	0.697
1	0.055	2.58	0.703	0.019	1.92	0.789	1.02	0.005	0.936	3.14	0.052	0.796	0.043	0.2	0.693
10	0.048	2.07	0.790	0.015	1.69	0.793	1.24	0.006	0.994	3.15	0.052	0.798	0.044	0.3	0.594
20	0.041	2.94	0.722	0.022	1.02	0.799	1.87	0.007	0.960	3.17	0.054	0.794	0.044	0.3	0.686
30	0.037	2.34	0.768	0.018	1.45	0.799	1.99	0.08	0.938	3.19	0.056	0.795	0.047	0.4	0.598
40	0.035	2.41	0.875	0.017	1.19	0.774	2.01	0.09	0.985	3.11	0.047	0.761	0.049	0.5	0.672
50	0.034	2.57	0.881	0.016	1.27	0.741	2.22	0.099	0.991	3.06	0.038	0.794	0.052	0.7	0.598

Table 3. Kinetic parameters at different Chloram concentrations and temperatures for the adsorption of Chloram on the surface of c-FD

Initial chloram conc. (mg/l)	Pseudo 1st order			Pseudo 2nd order			Intraparticle diffusion			Langmuir adsorption isotherm			Freundlich adsorption isotherm		
	K_1 (min^{-1})	q_e (mg/g)	R^2	K_2 (min^{-1})	q_e (mg/g)	R^2	K_{id}	c (mg/g)	R^2	q_{max} (mg/g)	K_L (l/mg)	R^2	K_F (mg/g)(l/mg)$^{1/n}$	1/n	R^2
0.001							0.984	0.004	0.999	3.12	0.049	0.787	0.039	0.2	0.695
0.01	0.057	2.59	0.704	0.022	1.96	0.788	0.998	0.005	0.997	3.15	0.054	0.798	0.043	0.2	0.698
1	0.058	2.60	0.706	0.021	1.93	0.790	1.03	0.006	0.965	3.17	0.053	0.799	0.045	0.3	0.694
10	0.049	2.09	0.792	0.017	1.72	0.795	1.27	0.007	0.997	3.18	0.055	0.799	0.045	0.4	0.596
20	0.044	2.97	0.727	0.025	1.32	0.799	1.88	0.008	0.963	3.19	0.057	0.795	0.047	0.5	0.687
30	0.039	2.36	0.770	0.019	1.48	0.797	1.99	0.09	0.941	3.20	0.059	0.798	0.048	0.5	0.598
40	0.038	2.43	0.877	0.018	1.22	0.776	2.03	0.10	0.987	3.14	0.045	0.767	0.050	0.6	0.674
50	0.037	2.59	0.884	0.019	1.30	0.745	2.27	0.11	0.995	3.09	0.039	0.798	0.054	0.8	0.598

Table 4. The thermodynamic parameters such as standard enthalpy change (ΔH°, kJ/mol), standard entropy change (ΔS°, kJ/mol.oK) and standard Gibbs free energy (ΔG°, kJ/mol), can be calculated and the parameters obtained

Adsorbent	**Temperature (ºK)**	**ΔGº (kJ/mol)**	**ΔHº (kJ/mol)**	**ΔSº (kJ/mol.K)**
c-FD	298.15	- 2.7680	- 39.553	- 0.0123
	308.15	- 0.1650		
	318.15	- 0.0419		
FD	298.15	- 0.3318	- 5.368	- 0.0169
	308.15	- 0.1628		
	318.15	- 0.0062		

Table 5. The removal efficiency of microorganisms from surface water at high and low Chloram concentrations with 2 mg/l Fe2O3–Dy2O3 nanocomposites (FD) after 15 min contacting time

Microorganisms			**İnitial Concentrations**	
E. coli			20.000 cfu/ml	
Pseudomonas			27.000 cfu/ml	
Salmonella			12.000 cfu/ml	
Enteric viruses			7650 cell/ml	
Chloram Concentrations (mg/l)	**E. coli (removal efficiency, %)**	**Pseudomonas (removal efficiency, %)**	**Enteric viruses (removal efficiency, %)**	**Salmonella (removal efficiency, %)**
0.0001	99	98	97	96
0.001	99	98	97	96
0.01	99	98	97	96
0.1	99	98	97	96
2	99	98	97	96
5	99	98	97	96
10	99	98	97	96
15	99	98	97	96
20	99	98	97	96
25	99	98	97	96
30	99	98	97	96
35	99	98	97	96
40	99	98	97	96
50	99	98	97	96
60	84	87	87	86
70	80	80	80	80
90	80	80	80	80